IEEE Access
Multidisciplinary | Rapid Review | Open Access Journal

Received 5 January 2024, accepted 11 January 2024, date of publication 15 January 2024, date of current version 23 January 2024.

Digital Object Identifier 10.1109/ACCESS.2024.3354372

SURVEY

Exploring Design Approaches for 3D Printed Antennas

SAÚL S. CARVALHO[1,2], JOÃO R. V. REIS[1,2], ARTUR MATEUS[1,3], AND RAFAEL F. S. CALDEIRINHA[1,2], (Senior Member, IEEE)

[1]Polytechnic of Leiria, 2411-901 Leiria, Portugal
[2]Instituto de Telecomunicações, 2411-901 Leiria, Portugal
[3]Centre for Rapid and Sustainable Product Development, 2430-028 Marinha Grande, Portugal

Corresponding author: Rafael F. S. Caldeirinha (rafael.caldeirinha@ipleiria.pt)

This work was supported in part by the Portugal PRR—Plano de Recuperação e Resiliência (The Recovery and Resilience Plan), under project INOV.AM; and in part by the European Union (EU) funds under Project 2020-2023-UIDB/50008/2020 e UIDP/50008/2020.

ABSTRACT This comprehensive review explores advancements in the design, fabrication and performance evaluation of three-dimensional (3D) printed antennas, across different frequency ranges. The review highlights the use of diverse printing methods, materials and structures, to achieve specific antenna characteristics and designs, such as wide bandwidth, high gain, circular polarization, and beamforming capabilities. Simulation and measurement results are compared to assess antenna performance, considering parameters such as impedance bandwidth, radiation patterns, gain, and efficiency. The findings showcase the significant potential of 3D printing in the development of antennas for wireless communications, terahertz fr equencies, transmitarray, and multi-beam systems. Various printing techniques are employed to fabricate antennas with complex geometries and optimized performance. Rigorous measurements validate simulation results, addressing challenges related to printing resolution and material selection. This review emphasizes the contributions of 3D printing in antenna engineering, offering customization capabilities, rapid 3D, and improved performance.

INDEX TERMS 3D printing, additive manufacturing, antenna, antenna design, fused deposition modeling, direct metal laser sintering, stereolithography.

I. INTRODUCTION

In modern wireless communication systems, antennas play a crucial role as they constitute a fundamental component in the systems that enable efficient signal transmission. Three-dimensional (3D) printing emerges as a promising solution to address the high costs and delivery times associated with conventional antenna fabrication, but also the possibility of exploring novel design forms or methods. The rapid growth of 3D printing in recent years has made related hardware, especially Fused Deposition Modeling (FDM), Stereolithography (SLA) and Direct Metal Laser Sintering (DMLS) printers, increasingly affordable and accessible for individuals, contributing to its widespread adoption. This rapid production technology offers versatility and finds applications across various industries, enabling rapid prototyping of both functional and decorative components.

Due to the remarkable intersection of these fields, there are reported in the literature cutting-edge antenna models, representing a disruptive approach to the design and manufacturing of essential components for wireless communication systems, satellite communication, radar systems, and beyond.

In the context of mass production, 3D printing can be leveraged to produce antennas that deliver comparable performance to their traditional counterparts, while incurring only a fraction of the original cost. Furthermore, for custom-tailored applications, where the antenna quantity is limited, conventional manufacturing methods would typically result in a steep increase in production costs. It also offers a cost-effective alternative in such scenarios.

In this article, we provide a concise overview of the use of different 3D printing categories, specifically focusing on their processes, in the fabrication of 3D printed antennas.

The associate editor coordinating the review of this manuscript and approving it for publication was Ravi Kumar Gangwar.

Our primary objective is to gain insights into the prevalent processes employed in the creation of these antennas, encompassing methodologies and strategies for design, simulation, optimization, and manufacturing. We aim to understand how these processes impact the development of 3D printed antennas throughout their creation. Additionally, we emphasize the importance of gathering data on antenna parameters during both simulation and post-fabrication phases. Data obtained from these measurements is essential for the validation of designs in each specific case study and application.

This paper is organized as follows: section II presents a historical insight about the evolution of the 3D printing technology. In section III there are presented the most common additive manufacturing methods (related to 3D printing) categorizing them according to the corresponding fabrication process as per existing standards. Some pros and cons for the most used techniques utilized in the fabrication of antennas are also presented in this section. Section IV is dedicated to an extensive literature review about 3D printing antennas presenting various design approaches, materials and fabrications methods. This section is subdivided according to the categories used for the production of the 3D printed parts that composed the proposed antennas. Finally, in section V are drawn the main conclusions.

II. A BRIEF HISTORY OF 3D PRINTING

Three-dimensional (3D) printing and additive manufacturing (AM) are often used interchangeably, but they refer to distinct processes. 3D printing involves depositing material in a specific pattern using a defined method to create an object, while additive manufacturing involves adding layers of material to build an object [1]. The term ''3D printing'' was not widely used until 1996, when Z Corporation marketed a process that involved bonding plaster powder with a binder [2]. While early attempts at 3D printing can be traced back to the end of the 19th century [3], it was not until the 1980s that the technology began to be refined, with multiple patents for 3D printing technologies being filed. In 1984, Charles Hull invents SLA, which is considered the first envisioned 3D printing technology. Hull is known as the ''Father'' of additive manufacturing and founded the first 3D printing company, which commercialized the first 3D printer, the SLA-1 [4]. In 1989, Carl Deckard's patent for Selective Laser Sintering (SLS) was approved, and he launched his startup, DTM Corp., while Scott Crump was developing the FDM process and founded Stratasys [3], [4].

During the 1990s, several new technologies emerged. Solidscape developed the Binder Jetting (BJ) technique in 1993, while at the same time, Soligen contributed with Direct Shell Production Casting (DSPC) [2]. In 1994, Electro Optical Systems developed DMLS, also known as Direct Metal Printing (DMP), and the Fraunhofer Institute developed Selective Laser Melting (SLM). Later in the same year, AeroMat invented Laser Additive Manufacturing (LAM) [4] and in 1998, Objet Geometries Ltd. was founded, introducing the PolyJet process. In 1999, Extrude Hone AM installed the first metal printer, the ProMetal RTS-300 [3]. The early 21st century saw expensive professional 3D printing machines mainly used in the industry, as only a few had the financial capability to acquire such costly equipment. However, as 3D printing technologies began to flourish and new techniques were developed, new projects emerged, such as RepRap, which gained recognition for providing a low-cost solution for Fused Filament Fabrication (FFF) using plastics like Polylactic Acid (PLA) as a printing filament. This filament was invented by Vik Olliver and helped to make 3D printing more accessible to a wider audience [3].

The availability of a low-cost solution paved the way not only for 3D printing communities focused on storing and sharing 3D models for objects and contraptions, but also for new 3D printing companies that shifted their business models to focus on domestic use scenarios. As a result, owning a 3D printer paired with a computer became a desirable and useful tool for solving many common problems that previously required complex equipment and expertise. Rapid 3D and iterating over various designs using an easy-to-use, inexpensive tool is now possible. The versatility of 3D printing processes enables them to be used in a wide range of industries and applications, including dentistry, medicine, education, architecture, arts, fashion, and even the food industry. Additionally, 3D printing has been used to fabricate functional electronics, such as passive elements like resistors, capacitors, inductors, traces/contacts, and antennas. Or used in the fabrication of active elements like transistors, batteries, LEDs, solar cells, flexible displays, sensors (for, temperature, humidity, gas detection, etc.) and actuators (thermally conditioned, magnetic-driven, piezoelectrically or optically activated). Examples of such applications can be found in [3] and [5].

III. ADDITIVE MANUFACTURING CATEGORIES

Thanks to standardization, the preceding methods can be consolidated into seven AM categories, in accordance with ISO/ASTM 52900:2021 [1], [3]. These categories, and some of their corresponding processes, are summarized in Fig. 1.

- Binder Jetting (BJT) - In this process, a liquid bonding agent is selectively sprayed to bond powder materials. The models are usually required to go through curing and then sintering techniques to achieve the required mechanical properties;
- Directed Energy Deposition (DED) - This process uses focused thermal energy, such as a laser, electron beam, or plasma arc, to melt materials as they are deposited. The deposited materials come in the form of wires or powders and are mainly composed of metals;
- Material Extrusion (MEX) - A filament or pellets are selectively dispensed through a nozzle or orifice in this process, as in a traditional 3D printing machine;
- Material Jetting (MJT) - Beads of granulated materials, such as photopolymer resin or wax, are selectively deposited;

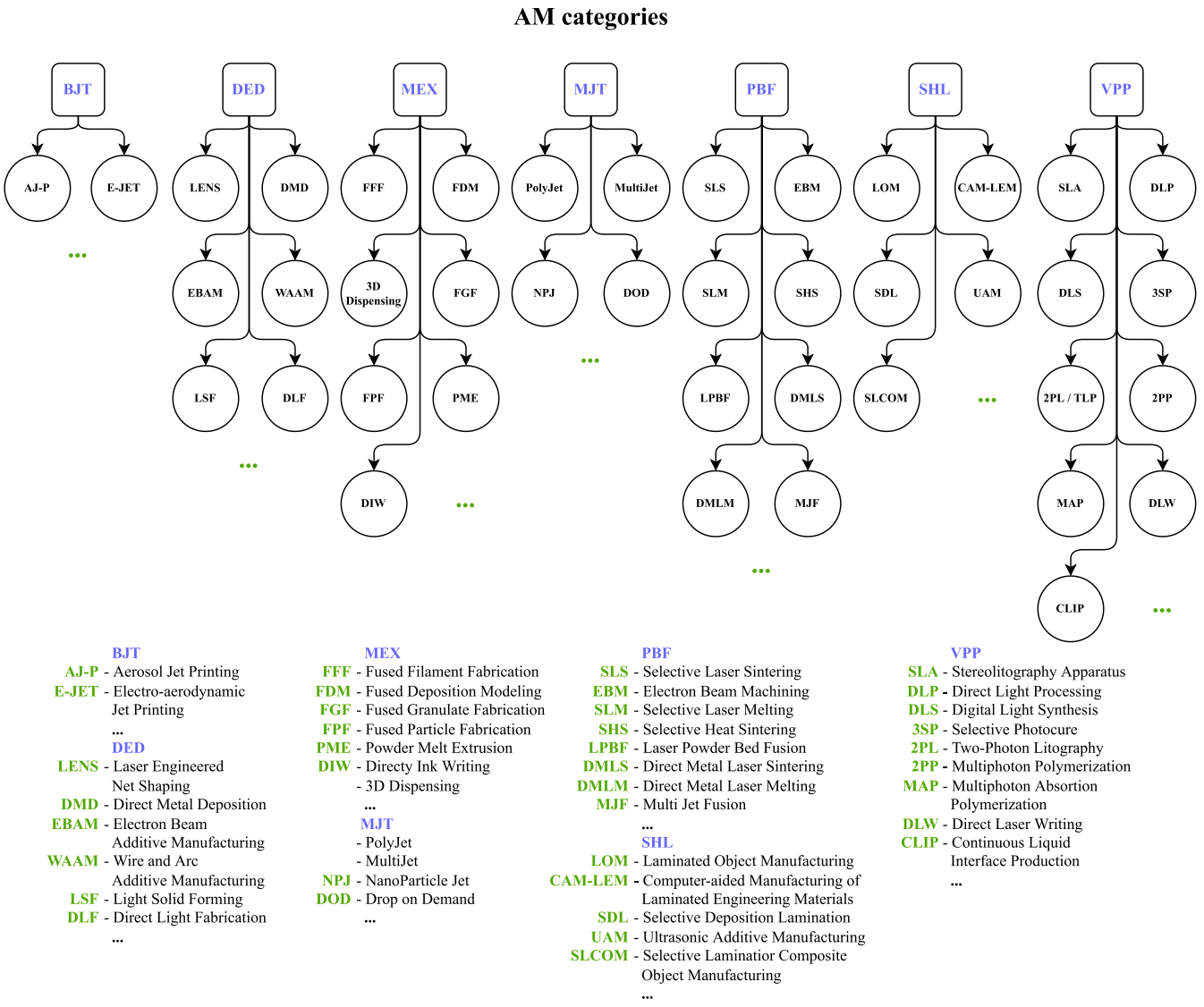

FIGURE 1. Classification of 3D printing methods under the seven AM categories.

- Powder Bed Fusion (PBF) - This process selectively fuses regions of a powder bed using thermal energy;
- Sheet Lamination (SHL) - In this process, sheets of a material are bonded to form a part;
- Vat Photopolymerization (VPP) - A liquid photopolymer in a vat is selectively cured using light-activated polymerization.

Among the seven AM categories, three stand out as particularly prominent for antenna fabrication, MEX, VPP, and PBF. The most commonly employed AM processes within these categories are respectively, FDM, SLA, and DMLS, briefly characterized below:

- FDM is a popular 3D printing technology that utilizes a thermoplastic filament. The filament is heated and extruded layer by layer to build a 3D object. This method is widely used in various industries for tasks such as rapid prototyping and manufacturing.
- SLA, or stereolithography, is one of the earliest and most commonly used 3D printing processes. It employs a laser to selectively cure and harden a liquid resin, layer by layer, resulting in the creation of a 3D part. SLA is renowned for its ability to produce highly detailed and precise prototypes and parts.
- DMLS is a specific 3D printing or AM technology primarily utilized to produce intricate metal parts and prototypes.

Since each AM category encompasses distinct processes, which themselves imply the use of different materials, it is important to follow specific rules for each type of material to achieve the best outcome for a 3D print. Common problems encountered in FDM/FFF, which are among the most widely used methods for 3D printing [3], include lack of structural support. For example, bridging occurs when the printer tries to join multiple structures with filament that are too far apart,

TABLE 1. Comparison of the most common 3D printing technologies used in antenna fabrication (table constructed from data presented in [5], [6], [7], and [8]).

Process	Advantages	Disadvantages
FDM/FFF	Low cost for machines and materials	Low resolution
	User-friendly	Limited detail
	Large build volume	Limited accuracy
	Wide range of filaments/granulates	Weak strength (between layers)
	May need support structures	High anisotropy
SLA	High resolution	Expensive equipment
	High detail	Hazardous chemicals
	Smooth surface finish	Parts can be brittle
	Wide range of resins	Limited build volume
DMLS	High accuracy and precision	May present surface roughness
	No support structures needed	May present porosity
	Very low waste of material	Residual stress
	Wide range of powders	Microstructural defects

causing the heated filament to bend with gravity and create a warped print. Lack of support can lead to catastrophic scenarios, as in FDM printing the printer prints layer-by-layer from bottom to top. If there are parts of the structure that only appear in the middle section of the object, the printer will try to deposit filament over the air, leading to unexpected situations such as nozzle clogging. This issue can be overcome by implementing structural supports such as tree supports. SLA and DMLS also have their own particularities and rules when it comes to Computer-Aided Design (CAD) model preparation and 3D printing setup. When applied to the fabrication of antennas, FDM/FFF, SLA and DMLS technologies have certain benefits over others. However, in certain cases, these processes may not be sufficient to achieve the required accuracy and attain the desired print quality for specific designs. A brief comparison of FDM/FFF, SLA and DMLS can be seen in Table 1.

3D printing processes rely on specific materials for part fabrication, they come on different formats and compositions. In the case of FDM/FFF 3D printing, which materials come in the format of a filament, PLA is the prevailing, followed by polyethylene terephthalate glycol (PETG), acrylonitrile butadiene styrene (ABS) and acrylonitrile styrene acrylate (ASA). PLA offers a diverse range of solutions, including special filaments such as conductive PLA and metal-infused PLA [7], which may prove valuable in creating specific antenna components. The advantages of using PLA are related to its low printing temperatures and low cost, while the 3D printed objects provide medium structural strength. But PLA has the downside that of break under physical stress and not being weather resistant (direct sunlight or rain weakens the parts) [7]. PETG advantages are that it is non-toxic, also easy to use, durable, weather resistant, but as disadvantages it may warp during printing, may stick firmly to the heatbed and needs to be strictly in a dry environment to improve filament lifespan [7]. This material tends to be more flexible than PLA. As for ABS and ASA, both materials exhibit excellent resistance to heat and UV light being suitable for outdoor applications. They typically offer more structural strength when compared with PLA or PETG filaments. However, a notable drawback is they demand for a consistent and relatively high printing temperature, depending on the use of an thermal enclosure to achieve the best print results [3]. In addition to filaments, 3D printing materials are available in various forms such as liquid polymers, powders, pellets, films, and gels. For instance, liquid polymers find application in the VPP and MJT categories, while metal powders, such as aluminum power (AlSi10Mg) are quite often used in DMLS to produce parts. As previously stated, the suitability of these materials for specific processes depends on their structural form. Laser Powder Bed Fusion (LPBF) exemplifies a manufacturing technique in which powders, including metals, polymers, and ceramics, are utilized. LPBF is a term commonly interchanged with SLM and DMLS, although subtle distinctions exist among them. LPBF serves as a more generic term, encompassing a broader range of materials, whereas SLM and DMLS specifically involve metals, and SLS is limited to polymers and ceramics. In SLM, powders undergo complete melting, resulting in the creation of a fully fused part. In contrast, DMLS involves the sintering of the part, which means it is partially melted. Consequently, the surface of the produced part in DMLS tends to be rougher compared to the smoother finish achieved in SLM. Shifting the focus to the broader context of 3D printing, it is important to explore not only the categories, processes and employed materials, but also the overall development and applications of this technology. In particular, the application of 3D printing antennas. The following section will provide a comprehensive overview of the subject matter. On Section IV, several antenna designs created through 3D printing processes are presented, highlighting the processes and materials considered for each development and presenting its main features, for comparison.

IV. 3D PRINTED ANTENNAS: A REVIEW

Recent studies have shown that modern 3D printing techniques are capable of reproducing entire metal, dielectric, or multi-material antennas as in comparison to traditional methods of fabrication. As an illustration, the fabrication of patch antennas, akin to microstrip antennas, involves a printing procedure that can be selectively applied to either the dielectric or conductive components, or even both [6]. This section provides a brief analysis and comparison of several antenna designs, using different methods of fabrication and taking into account different considerations during design, simulation and fabrication. This review is sub-sectioned according to the 3D printing technique utilized in the production of the antenna. The references are further summarized in Table 2.

A. FDM/FFF

The authors in [9] explored various techniques for 3D printing antennas using FDM, by exploring the properties of conductive filaments and by modifying the substrate properties with the printing infill. Microstrip transmission lines, patch

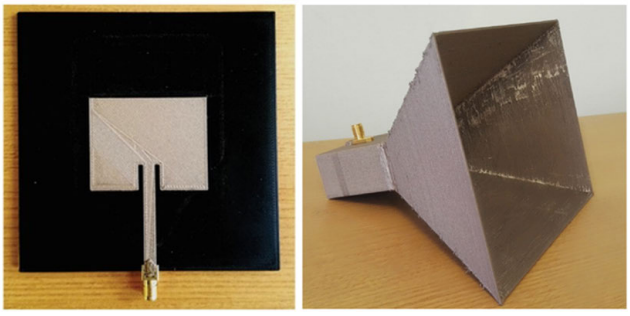

(a) (b)

FIGURE 2. (a) Microstrip patch in Electrifi filament over a PLA substrate and, (b) pyramidal horn in Electrifi filament (images extracted from [9]).

antennas, and a pyramidal horn antenna were fabricated using a modified Ocular 3D printer. The authors started by experimentally characterizing the dielectric properties of the considered thermoplastic materials using the transmission line method. Several prototypes have been produced by using the lines either made of thin copper foil or 3D printed in conductive filament (Electrifi), glued over 3D printed PLA substrates. Further tests were conducted by varying the infill percentage, layer height, and infill pattern for the transmission line. Losses were found to be similar between a PLA substrate with a copper foil-based transmission line and an FR-4 substrate with etched copper. According to the authors, the increase in the infill percentage reduces losses at higher frequencies, while no significant changes were observed below 4 GHz. The infill pattern had a greater impact at lower infill percentages, resulting in significant differences between two different patterns at higher frequencies. Lower layer heights generally resulted in lower losses. Subsequently, multiple patch antennas were fabricated, one using black PLA and Electrifi at 2.5 GHz (Fig. 2a), one with FR-4 and etched copper, and another with PLA substrate and copper foil patch. The measurements and simulations presented a good agreement, with all antennas exhibiting a maximum gain of approximately 3 dBi. Lastly, a pyramidal horn antenna was also printed using Electrifi filament, as depicted in Fig. 2b. The experimental results obtained with prototyped horn antenna was were compared with the ones obtained in simulations. The printed horn antenna presented a gain of 14.3 dBi at 5.8 GHz, with a difference of -0.7 dB, when compared to simulations. Such losses were associated to the surface roughness of its internal walls.

Article [10] presents a wideband multiple ring dielectric resonator antenna (DRA), fabricated for 6.15 GHz, using FDM 3D printing. The antenna consists of four concentric dielectric rings, while the center part is a solid cylindrical dielectric resonator and outer rings are made of ratios of dielectric and air. As shown in Fig. 3, the dielectric resonator (a) is mounted on a circular aluminum ground plane (b), creating the DRA (c). In the design phase, the effective permittivity (ε_{eff}) can be controlled by changing wall thickness of the dielectric resonator. The antenna was optimized in (High Frequency Simulation Software)

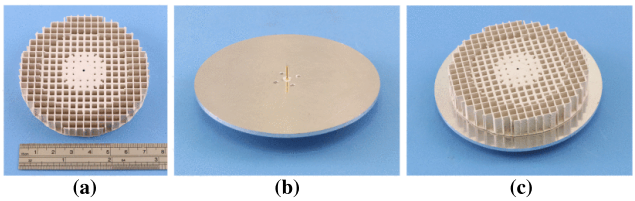

(a) (b) (c)

FIGURE 3. (a) Dielectric resonator, (b) aluminum ground plane with feeding probe and, (c) full assembly of the DRA (images extracted from [10]).

HFSS, a full wave electromagnetic solver, from which ε_{eff} was extracted, based on S-parameters. As for fabrication, the four dielectric rings were optimized, improving their individual values of relative permittivity (ε_r), for different thicknesses, with a printer whose resolution was 0.05 mm and 0.1 mm of tolerance. The measurements were done with a vector network analyzer (VNA) and a multi-probe system. The measured impedance bandwidth at -10 dB is 60.2% from 4.3 to 8.0 GHz, which is possible by merging the three resonant modes, at 4.7 GHz, 5.8 GHz and 7.2 GHz, where the E field has one, two or three half cycles along the x direction, accordingly. As for the radiation patterns, in each elevation plane, the co-polar field is stronger than its cross-polar counterpart by more than 20 dB, and for the each azimuth plane, by at least 18 dB, pointing that the DRA is good at providing vertical polarized radiation. The measured realized antenna gain varies between 0.65 and 2.45 dBi, with an average antenna efficiency of 89%, and a maximum efficiency of 95%, across the impedance band, from 4.3 to 8.0 GHz.

Multiple ultra-wideband microwave flat gradient index lenses were manufactured using the FDM/FFF process in [11]. The plane wave conversion is achieved in the lens due to its variable permittivity profile, which has a maximum value at the center and gradually decreases across the radius, so that all incident rays will have an equal phase when they exit the lens. The ε_{eff} of the lens rings can be adjusted by altering volume percentage, only depending on the ε_r of the 3D printing material used. Additional artificially engineered dielectric materials were used to increase the ε_r of the printed lens. This materials are constructed by adding metallic patches to the top and/or bottom of an additional dielectric sheet, which are then added to the lens element. The lenses were fabricated with a Makerbot 2X, using different materials, including ABS and PREMIX PREPERM TP20280. The dielectric properties of these materials were confirmed through prior testing with an X-band waveguide and the Nicolson-Ross-Weir method. Three lenses were printed (Fig. 4): one ABS lens printed in red filament, one yellow lens composed of three outer yellow ABS rings with varying infill factors and three inner rings made of 100% infill with slots, and lastly, composed of white PREMIX filament for the three inner rings to increase ε_r and three outer rings made of blue ABS. The blue lens acts as an equivalent dielectric to the produced yellow lens. Subsequent measurements were carried out on the prototypes, revealing

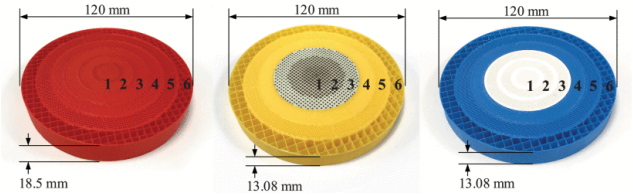

FIGURE 4. Prototype of the flat gradient index lenses with different material composition (images extracted from [11]).

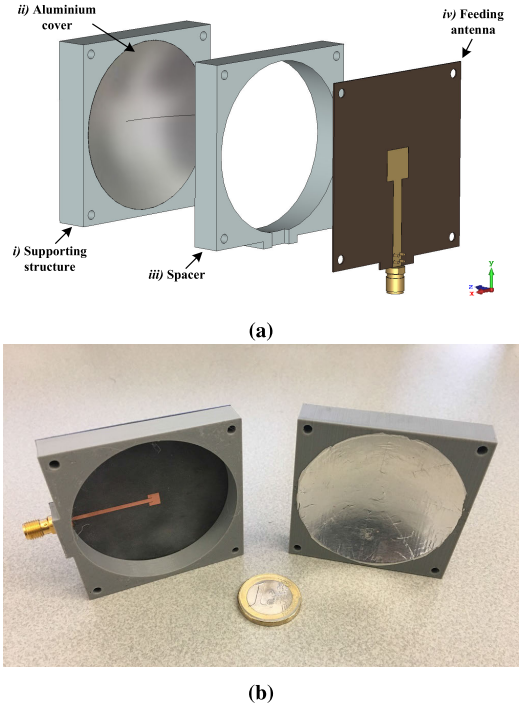

FIGURE 5. Compact parabolic reflector antenna: (a) schematic view and, (b) photography of the prototype (images extracted from [12]).

that the three lenses exhibited similar realized gains ranging from 15.1 dBi at 12 GHz to 23.6 dBi at 40 GHz, with efficiencies around 82%, while showcasing good wideband performance.

Recently, our research group has presented in [12] a FDM 3D printed solution for a compact parabolic reflector antenna aiming at radar applications in the K-eband. The proposed antenna is composed of four parts (Fig. 5a): (i) a paraboloid shape embodied in a supporting PLA material; (ii) a metallic coating applied to the paraboloid surface of (i), to enable it with electromagnetic reflecting properties; (iii) a PLA spacer that ensures the physical separation (i.e. focal distance) between parts (i) and (iv) and, finally, (iv) a microstrip patch antenna with a reduced ground plane to reduce feed blockage. After proper antenna optimization through electromagnetic simulations, the antenna has been fabricated and experimentally characterised in laboratory environment. The plastic parts were produced using a Creality Ender 3 printer, while the microstrip feeding patch has fabricated in a double-sided Rogers RT5880 substrate. The

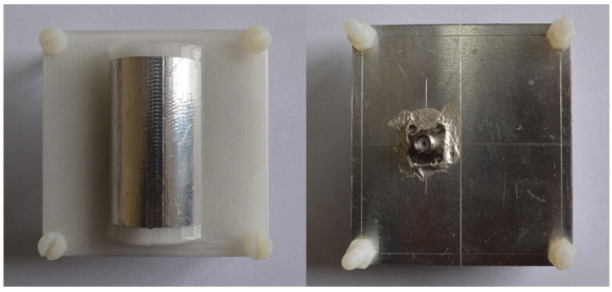

FIGURE 6. Fabricated curved patch antenna: (a) Top layer view and, (b) bottom layer view (images extracted from [13]).

metallization of the parabolic reflector was achieved by stamping two layers of aluminum foil with an approximate thickness of 20 μm, to ensure good shielding, trimmed and moulded to the shape of the parabolic surface. According to experiments realized on the prototype, the antenna exhibited a -10dB bandwidth defined between 23.5 and 25.5 GHz, verifying its operation in the 24 GHz ISM band, and 18.3 dBi of realized gain at 24.125 GHz.

The study presented in [13] introduces a curved 3D printed microstrip patch antenna designed to function at a frequency of 2.16 GHz, specifically intended for deployment in plastic CubeSats. The antenna structure, presented in Fig. 6 comprises two distinct sections: an upper layer housing a cylindrical protrusion made of ABS material with $\varepsilon_r = 2.3$ and $\tan\delta = 0.01$. On top of this, an aluminum patch is affixed, depicted in Figure 6. The lower layer, also constructed from ABS, includes an aluminum ground. Through simulations and optimization within CST Microwave Studio (CST MWS), the antenna's performance was assessed, followed by physical measurements conducted within an anechoic chamber using a VNA. The measurements exhibited a high degree of concurrence with the simulation outcomes. The antenna demonstrated a bandwidth of approximately 300 MHz, coupled with an radiation efficiency of around 96% across the entire band. Notably, the antenna's measured gain stands at approximately 6.7 dBi, while the cross-polarization (CP) levels were measured at around -20 dB. Impedance bandwidth was measured with about 300 MHz. Additionally, assessments were conducted to evaluate the material's thermal stability, employing techniques such as thermogravimetric analysis and differential scanning calorimetry. Complementary mechanical analyses were also carried out, including tensile tests and dynamic mechanical thermal analysis. The outcomes of these comprehensive analyses collectively endorse the fabricated antenna's suitability for deployment in the space environment, particularly within CubeSat platforms.

The authors in [14] introduce a 3D printed spiral dielectric leaky wave antenna that operates at 18 GHz. The antenna is depicted in Fig. 7. Unlike conventional designs, the radiating part of this antenna is entirely 3D printed. The antenna structure consisted of a grounded dielectric substrate with a ε_r of 3, and on top of it, a 3D printed Archimedean spiral with a higher, enabling right-hand

FIGURE 7. Bottom and top view of the 3D printed Archimedean spiral dielectric leaky wave antenna (images extracted from [14]).

circular polarization. To optimize the antenna's performance, the authors conducted parametric studies to determine the optimal thickness and ε_r of the 3D printed spiral. These findings unveiled that a spiral thickness of 2 mm with a ε_r of 10 yielded the best results. To fabricate the antenna, the authors have used PREPERM ABS300 and ABS1000 filaments for the grounded substrate and the Archimedean spiral, respectively. The antenna was then backfed with an SMA connector. The experimental results demonstrated good matching, an axial ratio, below 3 dB, within the 17.4 GHz to 19.18 GHz range, an impedance bandwidth around 16 to 20 GHz, a peak gain of 25 dBi at 18 GHz, a half power beamwidth (HPBW) of approximately 6°, and sidelobe levels (SLL) around −20 dB. In conclusion, the authors emphasized that employing 3D printing techniques offered design flexibility by enabling adjustments to parameters like thickness and, which significantly impact the antenna's behavior and performance.

In [15], a 3D printed wideband circularly-polarized multiple-input-multiple-output (MIMO) antenna operating at 10 GHz was fabricated. The antenna was constructed using two identical DRAs (dieletric resonator antennas), a dielectric decoupler, and a feed network. The FDM fabrication involved printing the dielectric resonator and decoupler in a single attempt, with different ε_r values to effectively reduce coupling in both E and H planes. Several approaches for the DRA's configuration were explored, including placing only the DRA's on the ground planes, using DRA's with the decoupler, and employing a two-layer decoupler with the DRA's, with the latter proving to be the most effective choice. To further enhance the axial ratio bandwidth, the upper layer of the decoupler was replaced with a polarizer composed of dielectric slabs, as seen in Fig. 8. After fabricating the antenna, measurements were conducted in laboratory environment. The results demonstrated good agreement with simulations, revealing an impedance bandwidths at −10 dB of 21.7%, spanning from 8.88 to 11.04 GHz, with an axial ratio bandwidth below 3 dB. The realized gain was found to vary from 4 to 5 dBic over the measured passband (8.88-11.04 GHz), with an efficiency exceeding 80% within

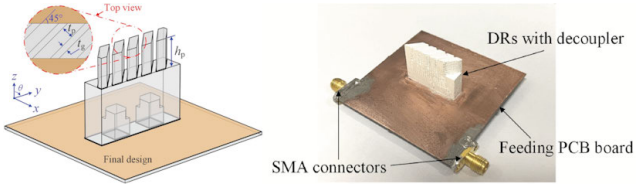

FIGURE 8. MIMO DRA: (a) final antenna design and, (b) fabricated antenna (images extracted from [15]).

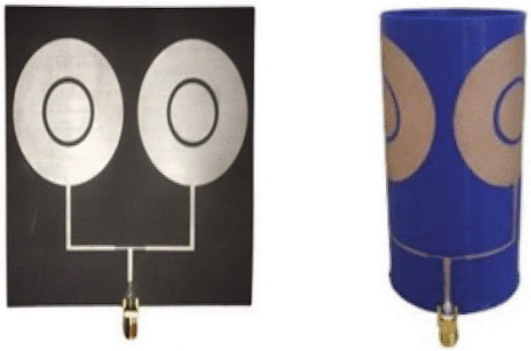

FIGURE 9. Greenfabricated CMA array: (a) in RT Duroid, and (b) in conformal PLA [16]).

the same frequency band. Additionally, measured mutual couplings were below -21.4 dB, indicating excellent isolation between the DRA's.

greenArticle [16] presents a FDM 3D printed dual-band energy harvester operating at 2.4 and 5.2 GHz, denominated as rectenna system. The rectenna is composed of a dual-band omnidirectional circular monopole antenna (CMA) array with a T-junction power divider, a Villard multiplier-based RF rectifier, and an impedance matching network. The rectenna is able to harvest RF energy as the antenna picks RF power, while the impedance transformer guarantees maximum power transfer and the rectifier converts the RF power to a DC voltage. The CMA array was first designed for a resonance at 2.4 GHz, with a circular patch, where a circular gap ring was introduced to achieve the second resonance at 5.2 GHz. The simulations were done for a flat RT duroid substrate (Fig. 9a) and a conformal PLA substrate (Fig. 9b) of $\epsilon_r = 2.57$ and $tan\delta = 0.02$ and a thickness of 0.787 mm. For the design of the rectifier circuit, low power, low turn-on rapid switching Schottky diodes (SMS-7630) were implemented, taking into account the characteristics of the RF signal. A two-stage Villard rectifier was built, allowing for rectification of the RF signal, followed by multiplication. After simulating the rectifier, the impedance matching network between the antenna and the rectifier circuit was calculated, based in the simulated input impedance of the two-stage rectifier. When measured at 2.4 GHz, the flat RT duroid substrate presented a bandwidth of 680 MHz and a peak gain of 6.6 dBi, while at 5.2 GHz, a bandwidth of 690 MHz and a gain of 6.4 dBi. For the conformal PLA substrate at 2.4 GHz, 700 MHz of bandwidth

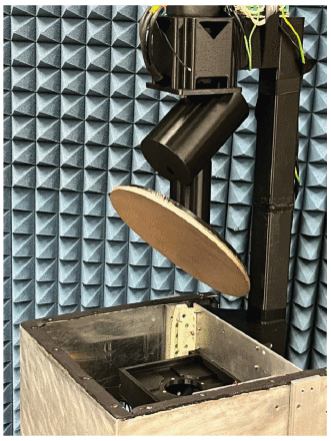

FIGURE 10. Greenassembled J-band FMCW radar system (image extracted from [17]).

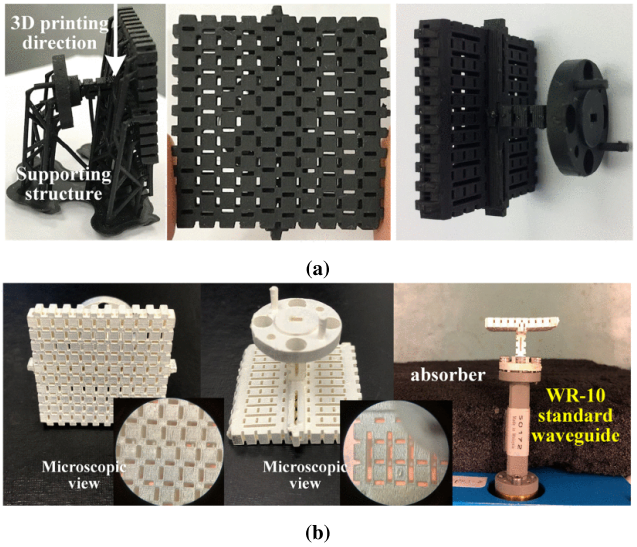

FIGURE 11. Fabricated SWAA: (a) 3D printed antenna and, (b) antenna after metallic coating (left and middle) and connected to WR-10 waveguide coupling (right) (images extracted from [18]).

were obtained with a peak gain of 5.7 dBi and at 5.2 GHz, a bandwidth of 570 MHz and a peak gain of 8.8 dBi. Conversion efficiencies were 67.29% with output of 1.39 V and 42.16% with output of 1.1 V for RF input power of 0 dBm at 2.4 and 5.2 GHz, respectively.

greenThe findings presented in [17] showcase a 223 GHz offset reflector antenna characterized by a geometry derived from a section of a closed elliptic toroidal surface. The reflector was integrated with a motor and various other RF components, culminating in the assembly of a J-band frequency-modulated continuous-wave (FMCW) imaging radar, depicted in Figure 10. The reflector specific geometry was chosen to achieve the narrowest beamwidth possible for a given aperture size. The reflector, a critical component of the radar, was manufactured using ABS filament on a Snapmaker 2.0 A350 3D printer. Unlike conventional approaches involving an acetone vapor bath for surface smoothing, another technique was employed. Initially, a coat of wood filler paste was applied to the reflector surface, followed by sanding to eliminate gaps resulting from the rasterization inherent in the FDM 3D printing process. Subsequently, the smoothed surface underwent a coating process involving ten layers of silver-coated copper spray, commercialized by MG Chemicals. Measurements were conducted in an anechoic chamber to evaluate the antenna's performance. The obtained results revealed a peak gain of 38.7 dBi. Furthermore, the HPBW in both elevation and azimuth were measured at 4.6° and 0.42°, respectively. These results indicated that the developed reflector antenna showed promising potential for radar applications in the high-frequency range, being particularly well-suited for high-resolution mapping in both outdoor and indoor scenarios.

B. SLA

The authors in [18] present a 3D printed W-band Slotted Waveguide Array Antenna (SWAA) using SLA. The SWAA design comprises a 10 × 10 slot array. The radiating slots were arranged non-uniformly to reduce SLL, while the non-radiating slots were angled to allow for metal spraying over the inner surfaces. The antenna was optimized using machine learning via an artificial neural network to improve its geometric design. A prototype of the antenna was produced in a Formlabs Form 2 printer and further metallized using silver jet metal spraying. Figure 11 displays the fabricated antenna before (a) and after metallization (b). The produced antenna was characterized in laboratory environment. The measured S_{11} presented a +0.68 GHz shift from the original 78 GHz frequency, resulting in −18 dB at the resonance frequency. According to the authors, this shift may have been caused by structural bending. This characteristic also led to changes in other parameters, including a decrease in gain to 22.5 dBi (−1.9 dB), an increase to 10° (+2°) in HPBW, and an increase of the SLL in 2.9 dB. In addition, the authors have assessed surface roughness using a profilometer and three samples were obtained with values of 9.9, 14.4, and 9.5 μm. A modified Huray model was utilized to determine the impact of the surface roughness, where a 2.4 dB gain reduction was found due to conductive loss.

In [19], a modified Fresnel Zone Plate Antenna (FZPA) operating at 300 GHz is presented. The lens consists of a subwavelength discrete dielectric posts in the odd-numbered Fresnel zones, produced using SLA technique. The lens was then constructed using periodic sheets of dielectric and air, forming an anisotropic metamaterial. The used dielectric material was a high-temperature resin with $\varepsilon_r = 2.66$ and loss tangent ($\tan\delta$) of 0.03 at 300 GHz, fabricated with a Formlabs Form 2 printer. To achieve a gain of approximately 27 dBi for the FZPA, nine Fresnel zones were selected along with other essential parameters. Figure 12 depicts the antenna prototype and the experimental setup for laboratory characterization. The measured S_{11} exhibited values smaller than −13 dB from 265 to 320 GHz. The cross-polarization levels were found to be more than 20 dB below the main beam. A 90° phase was observed at the central region,

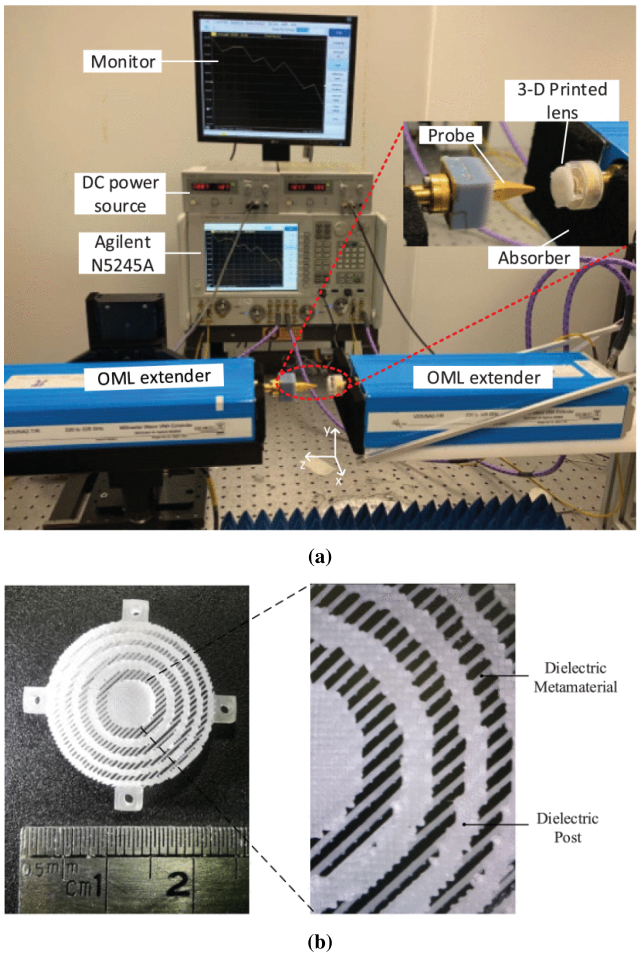

FIGURE 12. (a) Measurement setup for the fabricated lens and, (b) gabricated modified Fresnel lens through the authors approach (images extracted from [19]).

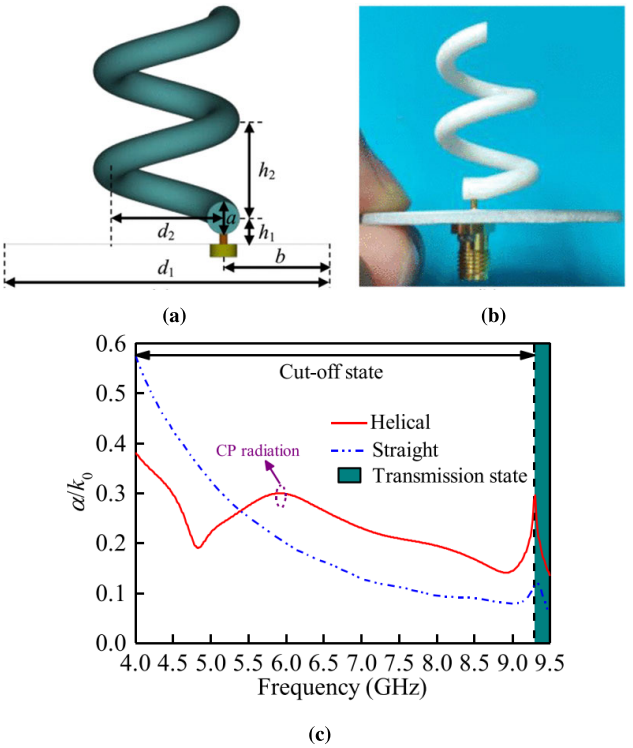

FIGURE 13. Helical antenna: (a) Prototype design, (b) fabricated antenna and (c) simulated normalized leakage constant (α/k_o) (images extracted from [20]).

indicating favorable CP radiation of the printed lens. The measured gain at 300 GHz was 27.4 dBic, with an aperture efficiency of 15.4%, a 3 dB gain bandwidth exceeding 15.1% from 275 to 320 GHz, and a 3 dB axial ratio bandwidth above 18.8% from 265 to 320 GHz. To conclude, the modified Fresnel lens provides increased phase correction capabilities compared to the conventional FZPA. However, it should be noted that at terahertz (THz) frequencies, improving radiation performance poses a challenge due to manufacturing limitations imposed by materials, structures, and designs that cannot be readily applied at lower frequencies.

In [20], a 3D printed helical antenna operating at 6 GHz was created using zirconia ceramic through the Ceramic SLA method. The authors started with simulations studies on a straight rod that was further curved into a helical shape. A comparison was made between the propagation constants, including the leakage (α/k_o) and phase constant (β/k_o) of the straight and helical models. According to the authors, the leakage α/k_o in the straight model gradually decreases with the increasing of the operating frequency, until the transmission state. However, in the helical model, the curve of α/k_o exhibited the similar tendency to that of the straight, one except an extra ripple appears in the cut-off state region, as depicted in Fig. 13c. This ripple coincided with the frequency band for the cross-polarization radiation, and it is caused by the bending process. The authors concluded that the helical diameter determines CP operating frequency or the position of ripple.

For the helical antenna design, three different geometries were created, all consisting of a helical element and a ground plane, with the only difference being their composition: fully metal, dielectric helical antenna with a metal ground, or fully made of zirconia. Simulations demonstrated that the zirconia antenna with a metal ground exhibited the best overall performance, radiating CP waves and having similar gain as a complete metal antenna while maintaining a low radar cross section at high frequencies. To fabricate the helical antenna, a CERAMAKER printer was used to produce it from >95% zirconia ceramic, while a 2 mm thick aluminum was used for the ground plane, as shown in Fig. 13b. After fabrication, the simulation results and measurements were compared, demonstrating good agreement for the radiation patterns and S_{11}, indicating a measured impedance bandwidth from 4.75 to 9.5 GHz. Radiation efficiency was about 95%, and the gain was around 10 dBic. The proposed antenna design benefits from the ceramic structure, leading to higher radiation efficiency, as there is no conductor loss.

In the sequence of the work [20], the same research group introduced in [21] a zirconia ceramic antenna manufactured using 3D printing technology. In contrast to traditional approaches employing full metallic components, this antenna

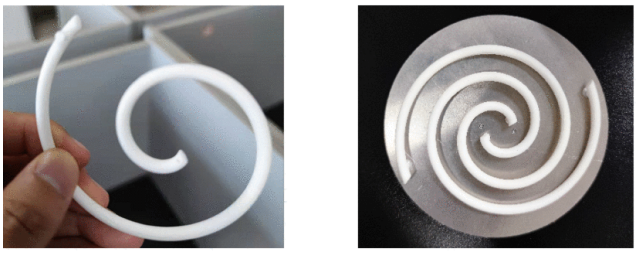

(a) (b)

FIGURE 14. Fabricated antenna: (a) 3D printed zirconia spiral arm and, (b) complete zirconia Archimedean spiral antenna (images extracted from [21]).

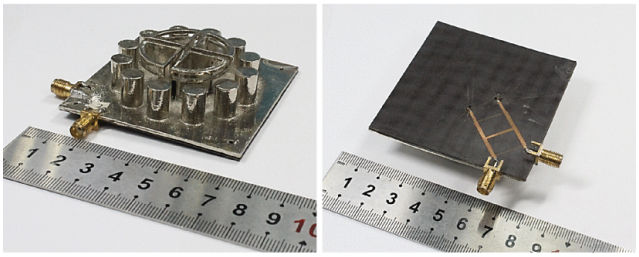

(a) (b)

FIGURE 15. Fabricated dual-CP antenna: (a) Top view of the dual-CP ME dipole and, (b) bottom view of the hybrid coupler (images extracted from [22]).

showcased a configuration with dual spiral arms crafted from zirconia ceramic, as depicted in Figure 14, along with an accompanying ground plane that finalized the design (b). The researchers aimed to compare the performance of the ceramic antenna with its metal counterpart through simulations. Following the simulation phase, the antenna was fabricated using a SLA employing a PCPrinter DLP96F printer. Subsequent measurements were carried out to validate the antenna's performance. The measurement results exhibited a favorable agreement with the simulations, although minor deviations were observed in the passband. The antenna showcased an impedance bandwidth spanning from 4.65 to 6.23 GHz, with an associated axial ratio bandwidth ranging from 4.75 to 6.1 GHz. The realized right-hand circular polarization gain remained below 9 dBic, and an impressive radiation efficiency exceeding 92% was achieved.

The authors of [22] developed a dual cross polarized magnetoelectric (ME) dipole antenna, which was created using SLA 3D printing with VeroPureWhite resin. The antenna consisted of three main layers: a 1 mm thick F4B substrate with $\varepsilon_r = 3.5$ and $\tan\delta = 0.001$, printed copper and chromium foils with a thickness of approximately 35 μm and 7 μm, respectively. These foils were added to the printed structure. The antenna itself was essentially an ME-dipole divided into four elements. On the top side of the substrate, a square ground plane was printed, while the bottom side houses the hybrid coupler for the dual cross polarized antenna, as depicted in Fig. 15. It was fed by orthogonal Γ-shaped strips that were printed over the dielectric-feed skeleton, with an air gap providing isolation between the two feeds. The hybrid coupler feeding network generates orthogonal signals with a phase difference of $\pm 90°$. To achieve a widebeam ME-dipole, twelve meta-columns and folded dipoles were combined with the conventional ME-dipole. The design was simulated and optimized in HFSS, while the S-parameters were measured using a VNA inside a far-field chamber. The antenna demonstrated an effective bandwidth of 51% from 3.2-5.4 GHz, a gain of 6.0 dBic at 3.4 GHz, a HPBW of 108° at both the xz and yz planes, and a radiation efficiency of 94%. Finally, the produced antenna was arranged in a 2×2 array with a more complex dual-feed network to enhance gain. Measurements were conducted on the array, obtaining an effective bandwidth of 48% from 3.2-5.2 GHz, a gain of 14 dBic at 3.4 GHz, and HPBW values of 44.2° and 43.8° at the xz and yz planes, respectively. The radiation efficiency was measured to be 88%. The obtained results affirm the antenna's potential as a promising candidate for 5G communications.

The article [23] presents a multibeam antenna operating at a frequency of 39 GHz, and illustrated in Fig. 16. The antennas consisted of a lens and an antenna array. The array was composed of a multiport linearly dual-polarized microstrip arrangement, employing a two-layer substrate. The top patch layer was crafted from CuClad217 substrate, while the bottom feed network layer utilized RT/duroid 5880. The lens underwent thorough simulation and optimization prior to fabrication. It was produced using SLA printing, employing FormLabs High Temp resin with properties $\varepsilon_r = 2.66$ and $\tan\delta = 0.03$, and then integrated into the antenna array. Experimental measurements were carried out within an anechoic chamber. Although there are an alignment between measurements and simulation, some deviations were observed, particularly in the measured SLL, with one of the levels exhibiting -10.2 dB (7.8 dB worse). The 3 dB gain bandwidth was measured at 12.3%. In absence of the lens, the measured gain stood at 6.5 dBi, while with the lens, for individual beams it ranged from 14.5 to 15.8 dBi, depending on the selected feeding patch. The directivity spanned from 17.8 to 18.4 dBi, corresponding to an aperture efficiency within 26.2% to 30.8%. The authors also highlighted that the antenna design was particularly suitable for intersatellite communication in CubeSat constellations due to its ability to generate beams in 16 distinct directions.

The research paper [24] details the development of a multibeam antenna operating at 355 GHz, utilizing a subterahertz metallic gradient index lens. This antenna design incorporated a surface-wave Luneburg lens positioned on a bed of nails, along with a feeder array comprising nine WR-2.2 waveguides. The feeding array can be divided into two components: firstly, waveguide grooves that are 3D printed along with the lens using an SLA nanoArch S140 printer and HTL resin, as depicted in Fig. 17; secondly, the cover was produced through CNC machining. Following the 3D printing process, a 500 nm gold coating was applied to the surface using magnetron sputtering, as illustrated in Figure 17b. After fabrication, the antenna's performance was

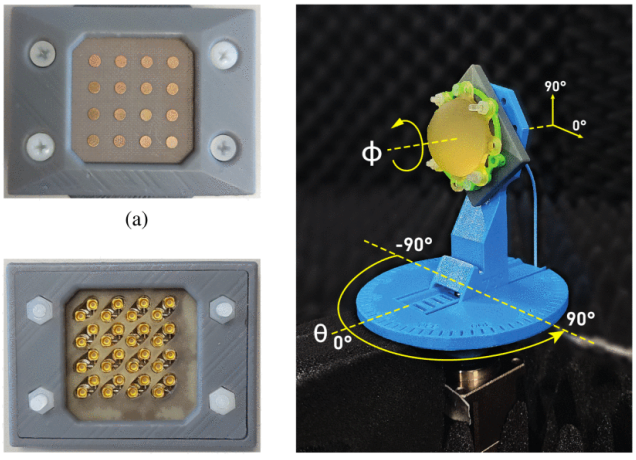

FIGURE 16. Fabricated antenna: (a) Patch top layer view, (b) feed network bottom layer view and, (c) complete antenna setup (images extracted from [23]).

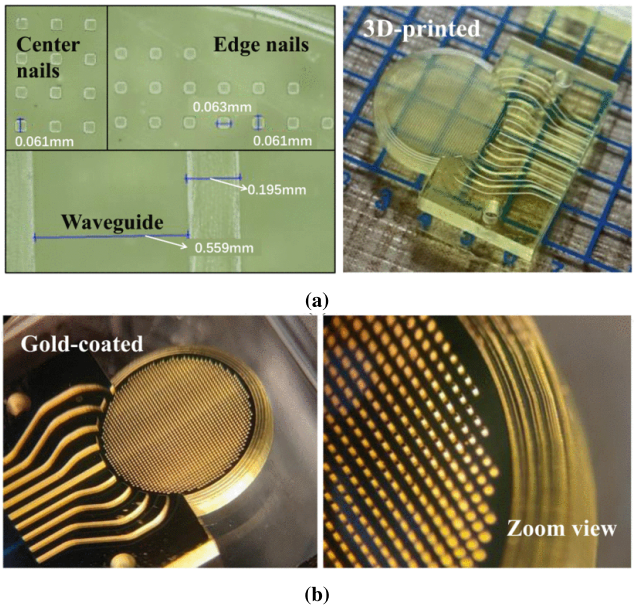

FIGURE 17. Fabricated GRIN antenna: (a) After 3D printing and, (b) after gold sputtering (images extracted from [24]).

evaluated using a VNA and range extenders, demonstrating favorable alignment with simulation results. The antenna exhibited mutual couplings between ports below −30 dB within the 350 to 360 GHz frequency range, reflection coefficients lower than −12.5 dB, and H-plane HPBW ranging from 5.7° to 6.3°. Notably, this antenna can achieve beamsteering within a range of ±60°. The realized gains at specific angles, including 0°, 15°, 30°, 45°, and 60°, were measured at 17.3 dBi, 17.1 dBi, 16.7 dBi, 16.4 dBi, and 16.1 dBi, respectively.

C. AEROSOL JET PRINTING

Remarkably, the work in [25] describes the fabrication process of two patch antennas for removable fingernails, utilizing the Aerosol Jet Printing (AJ-P) method, for microwave and mm-wave frequencies of 15 and 28 GHz,

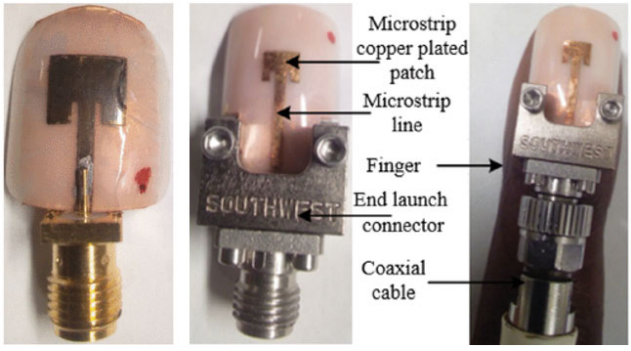

FIGURE 18. Fabricated patch antennas: (a) 15 GHz nail patch and, (b) 28 GHz nail patch (images extracted from [25]).

respectively. The microstrip patch was made with Cabot CS-32 nanoparticle silver ink, which was fabricated with an Optomec printer and cured with a NovaCentrix PulseForge. Simulations were performed in CST MWS, with the nail substrate made of ABS, having a thickness of 0.5 mm, $\varepsilon_r = 2.7$, and $\tan\delta = 0.0051$. The simulation accounted for different materials, as in bone, fat, skin, and nail tissues, each having different ε_r values and thicknesses. Both antennas were prototyped (Fig. 18) and experimental characterized. For the microwave antenna, the measured S_{11} is in good agreement with one obtained in simulations, albeit with a slight shift in the resonance frequency and a decrease in the −10 dB bandwidth from 9.8% to 9.1% for both on-finger and off-finger measurements. The bandwidth for the on-finger antenna spanned from 14.5 to 15.9 GHz. Radiation patterns were also obtained, presenting a 6.4 dBi gain in boresight and 70% efficiency. For the 28 GHz antenna, a copper layer was added to the silver layer through electroplating, while the ground plane was made of a copper tape on the underside of the nail. Surface roughness was observed with a microscope, revealing a 0.8 μm profile. The on-finger measurements showed a slightly wider bandwidth (26.9 to 29.8 GHz) compared to the off-finger measurement, with improved matching. Radiation patterns were also in good agreement with the simulation, exhibiting a 7.4 dBi gain and 80% efficiency. According to the authors, the nail antennas serve both as a functional ornament and a potential application for Internet-of-Things (IoT), particularly when installed on all fingers to form an array.

greenIn the work presented by [26], an aperture-coupled stacked patch array antenna (SPAA) was crafted from low-temperature co-fired ceramic (LTCC). This antenna operated within the D-band and was designed with a multi-layered structure, comprising four layers of LTCC (S1-S4) and five metal layers (M1-M5). The antenna architecture included a broadband transition from a grounded coplanar waveguide line to a microstrip line in layers M2 and M3, interconnected by vias. Following this transition, an impedance transformer and an open stub were incorporated. On the subsequent metal layers, an aperture (M3) was strategically positioned, followed by a patch (M4). The aperture served to couple

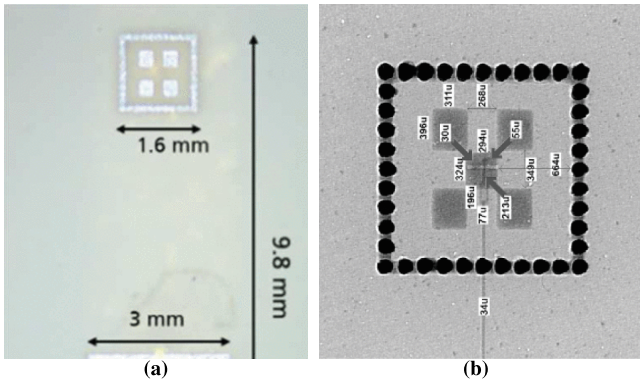

FIGURE 19. GreenFabricated LTCC SPAA: (a) Sintered LTCC setup and, (b) X-ray images of the SPAA (images extracted from [26]).

the energy from the feed line to the patch located above it. At the topmost metal layers (M5), four symmetrical patches were placed, all excited by the single patch below. This configuration introduced an additional resonance, effectively broadening the antenna's bandwidth and enhancing its gain. To confine the active region of the antenna, via fences were added, extending from the top layer (M5) to the feed layer (M2). The LTCC layers were fabricated using Ferro A6M-E, while the metal layers were printed atop each LTCC layer, created by AJ-P 3D printing technique. Subsequently, the antenna underwent a sinterization process and was verified using X-ray imaging, as illustrated in Figure 19. To further improve the beam shaping of the SPAA, an elliptical lens was 3D printed and placed atop the antenna. In the absence of the lens, measurements revealed a peak realized gain of 7.1 dBi, directivity of 7.6 dBi, an impedance bandwidth of 35 GHz, and a total efficiency of 88%. With the lens in place, the peak gain could be elevated to 18.9 dBi, accompanied by a directivity of 23 dBi. However, this enhancement comes at a cost of 10% reduction in total efficiency.

D. POLYJET

In the work [27], a three-layer dielectric structure was utilized to create a transmitarray antenna unit-cell element. The unit-cell was designed to improve bandwidth by adapting the characteristic impedance to the free-space impedance using tapered transmission lines. The unit-cell was made of RT-Duroid 6006 with $\varepsilon_r = 6.15$ and $\tan\delta = 0.0027$. Simulations were performed in CST MWS, leading to the definition of the unit-cell and to the creation of three different-sized TA antennas (TA1, TA2, and TA3) at 30 GHz. TA1 exhibited the lowest overall gain of 27.1 dB, while TA2 and TA3 had gains of 31.1 dB and 33.6 dB, respectively. However, TA1 had a wider -1 dB bandwidth of 30.9%, while TA2 and TA3 had narrower bandwidths of 27.4% and 17.5%, respectively. The HPBW in both H and E planes varied accordingly: (6.1°, 6°) for TA1, (4°, 4°) for TA2, and (2.9°, 2.8°) for TA3. The aperture efficiency was 41.4%, 45.3%, and 17.5% for TA1, TA2, and TA3, respectively. Modifications were employed to adapt the design to the physical capabilities of the 3D printer. A fourth TA design was then fabricated

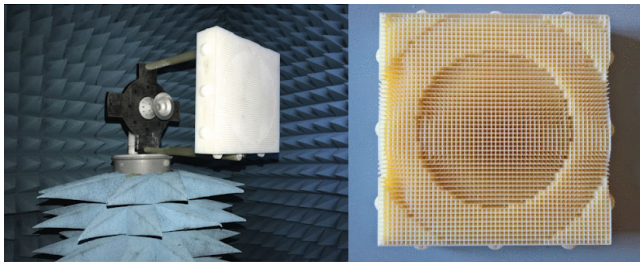

FIGURE 20. Fabricated TA: (a) Mounted in the anechoic chamber and, (b) top view after fabrication (images extracted from [27]).

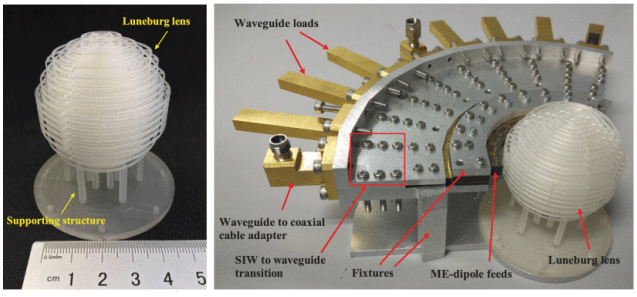

FIGURE 21. Fabricated prototype of the multibeam 3D printed Luneburg lens: (a) 3D printed Luneburg lens and, (b) lens with waveguide adapters and loads (images extracted from [28]).

using a PolyJet Objet30 printer and VeroWhitePlus resin, as seen in Fig. 20(b). Measurements were conducted in an anechoic chamber, with the TA mounted as presented in 20a, revealing a gain of 30.7 dBi, an aperture efficiency of 38.6%, and a -1 dB bandwidth of 21.5%. In conclusion, the study highlighted the limitations of additive manufacturing technologies, particularly at high frequencies, including the limited availability of materials with suitable dielectric properties and the low resolution of 3D printers. The authors emphasized the need for the development of new materials to overcome these challenges.

The paper [28] presents a 3D printed multibeam Luneburg lens for the Ka-band, utilizing a ME-dipole with endfire propagation. The lens was created through PolyJet process, and composed of a gradient-index spherical structure made of a mix of printing material and air, divided into multiple rings with varying ε_r. The challenge lied in finding a suitable printing material with a ε_r between 1 and 2 for mm-wave frequencies, while available polymers have a ε_r of nearly 3 or higher. Three types of structures were printed using VeroClear resin, namely a dielectric rod (A), slot (B), and lattice (C), with a $\varepsilon_r = 2.9$ and $\tan\delta = 0.01$ at mm-wave frequencies. The authors found that types B and C were able to reduce ε_r to around 1.3, while type A reduced it to approximately 1. The multibeam Luneburg lens, depicted in Fig. 21, was specifically designed with nine feeding elements in the xy plane. The most optimal arrangement was achieved when these elements were spaced 14.5° apart. The lens was 3D printed and measurements were conducted in the prototype. Radiation patterns were measured at 26.5, 32, and 38 GHz, and demonstrated similar performance to the

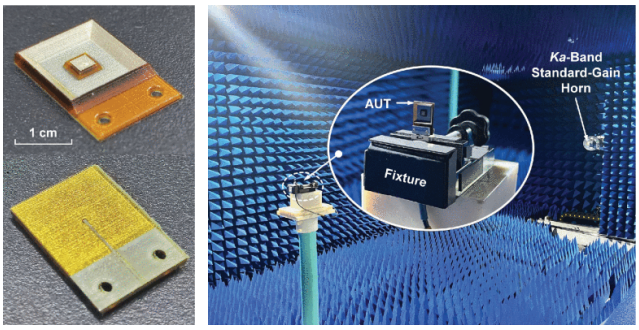

(a) (b)

FIGURE 22. GreenCavity-backed patch antenna: (a) manufactured antenna, and (b) measurement setup (images extracted from [29]).

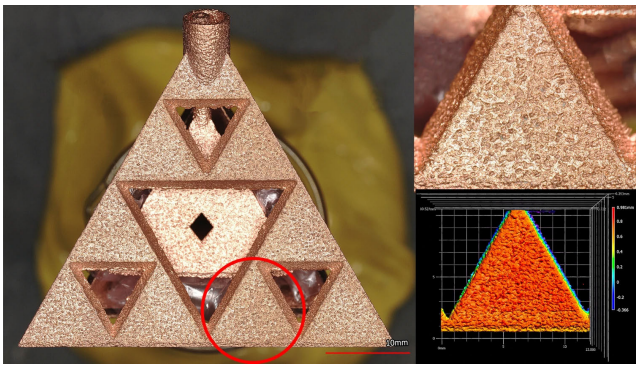

FIGURE 23. GreenFabricated copper pyramidal fractal antenna (left) and 3D optical profile (right) (image extracted from [30]).

simulations when the input ports were excited separately. The nine beams can cover a range of ±61°. The lens exhibited an operating bandwidth of 40% (at −10 dB), a crossover level from −2.6 to −5.5 dB, and an antenna efficiency ranging from 35 to 49%. The results for gain are very close to the simulated values, with a peak gain of 21.2 dBi, with a variation of the gain less than 2.5 dB over the operating band. The decrease in gain may be attributed to the dielectric loss of the 3D printed structure due to the material used, while the crossover level may be improved by using substrates with higher ε_r for the feed element.

greenThe study conducted in [29] introduced a monolithically integrated millimeter-wave quasi-planar cavity-backed patch antenna, fabricated through PolyJet technology and designed for operation in the Ka-band. Initially conceived as a simple square patch, the antenna design underwent further enhancements. A square dielectric-filled backed cavity was incorporated, shaped into a trapezoidal cross-sectional profile. The cavity underwent a selective hollowing process, subsequently being filled with air. To optimize antenna gain, the height of the cavity was then increased. The sidewalls and bottom face of the backed cavity were fully metallized, establishing reflective boundaries that effectively suppress back radiation from the patch antenna. The patch itself was backfed using a metal probe inserted from the back cavity. This probe penetrated the dielectric platform and connected to a feeding microstrip line on the rear side. The microstrip transitioned to a segment of 50 Ω grounded coplanar waveguide, facilitating compatibility with an end-launch RF connector. In the simulations, the dielectric and metal components of the antenna were modeled using acrylate polymer and silver, respectively. The silver's conductivity was set to 12.6 MS/m, as specified in the datasheet. The fabrication of the antenna involved PolyJet printing with ultraviolet-curable acrylate polymer and silver nanoparticle conductive inks for the dielectric and metal parts, respectively (Fig. 22a). During measurements in the anechoic chamber (Fig. 22b), the antenna exhibited an impedance bandwidth ranging from 26.9 to 31.7 GHz, with a corresponding gain of 5-7.8 dBi within the same frequency band.

E. LPBF

greenIn the study [30], a copper pyramidal fractal antenna was manufactured using LPBF 3D printing technique. The antenna's design was based in a 3D Sierpinski gasket configuration, incorporating a unique arrangement where a radiator was nested within a 3D ground plane in the shape of a gasket. This design maintained the alignment of the ground plane pyramid symmetrically at the center of a radiating pyramid. To approximate the dielectric properties of the non-conductive supports, typical thermoset values were employed in conjunction with known values of the copper conductor, as simulated in the study. Specifically engineered for optimal performance within the 5 GHz range, the radiation characteristics of the antenna were confined to the C-band for evaluation purposes. The fabrication process utilized Hoegenaes Cu OFCH powder, and a Trumpf TruPrint 1000 Green Edition LPBF printer was employed. Post-fabrication, the dimensional aspects and surface roughness of the antenna were measured. A Faro Quantum S ScanArm 3D scanner and a Keyence 3D Optical-Profilometer-VR-5000 were utilized for this purpose, as depicted in Figure 23. The observed roughness was found to be irrelevant to the operating frequency of the antenna. The DC conductivity of the copper printed components was determined using a Fischer Sigmascope SMP350, revealing an electrical conductivity of 58 MS/m and a thermal conductivity of 400 W/m·K. Subsequent measurements indicated a resonance frequency of 5.569 GHz, however, a less satisfactory match of −9.323 dB for the S_{11} was noted. Further investigations are to be employed, to explore additional performance parameters such as gain, efficiency, and radiation pattern, providing a comprehensive understanding of the antenna's overall performance.

The article referenced as [31] presents a LPBF 3D printed compact Conformal Slotted Waveguide Array Antenna (CSWAA), designed to operate at 14.5 GHz. The proposed antenna is shown in Fig. 24a and consists of a curved metallic body with slots, which is fed by an SMA connector. Simulations and optimization were conducted to determine the ideal design parameters, including slot width, slot length, and body conformity, in order to achieve maximum return

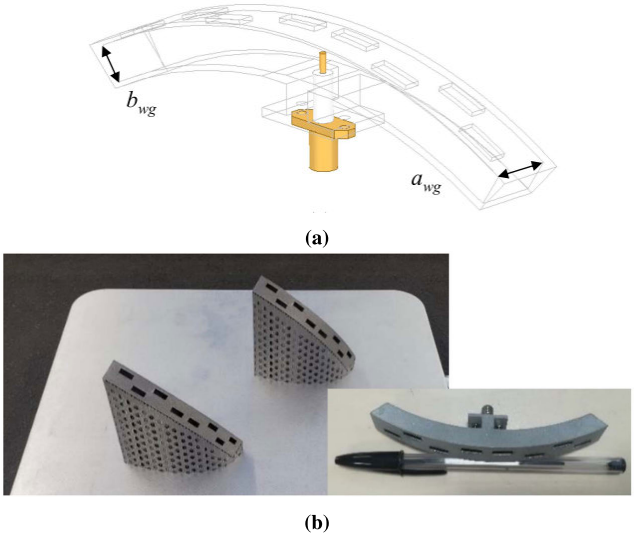

FIGURE 24. CSWAA antenna: (a) Example of 4 × 5 CSWAA with a beamforming network and, (b) fabricated CSWAA element (images extracted from [31]).

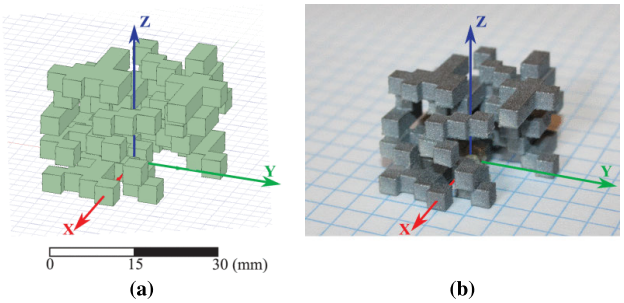

FIGURE 25. GreenEvolutionary optimized WiFi antenna: (a) Simulated antenna and, (b) fabricated antenna (images extracted from [32]).

losses and realized gain within a bandwidth as low as 5%. After the optimization process, two element prototypes of the CSWAA were fabricated, as seen in Fig. 24b, by using a LPBF printer, AddUp Formup350, and aluminum powder (AlSi10Mg). These prototypes were then machined to remove any remaining support structures. To validate the performance, measurements were conducted in an anechoic chamber, and the results showed good agreement with the simulations. Specifically, the S_{11} parameter remained below −10 dB across the 13.75 to 15 GHz frequency range, with a gain exceeding 14 dBi. The total and aperture efficiencies were measured at 90% and 50%, respectively, over the same frequency range. To address manufacturing challenges, the CAD model of the antenna was rotated 45° both around the x-axis and the y-axis, which helped prevent overhangs larger than 45° angles. In conclusion, the authors emphasized that this particular antenna design holds promise for applications in airborne and missile systems.

greenFurthermore, the study conducted in [32] outlines the development of 3D printed LPBF WiFi antennas, optimized through an evolutionary approach utilizing a genetic algorithm. A MATLAB environment was employed for the design and optimization processes, as illustrated in Figure 25a. In the genetic algorithm, a series of

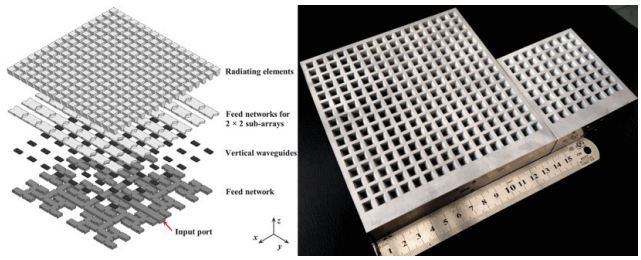

FIGURE 26. Horn antenna array: (a) Geometry of the antenna and, (b) 8 × 8 and 16 × 16.3D printed prototypes (images extracted from [33]).

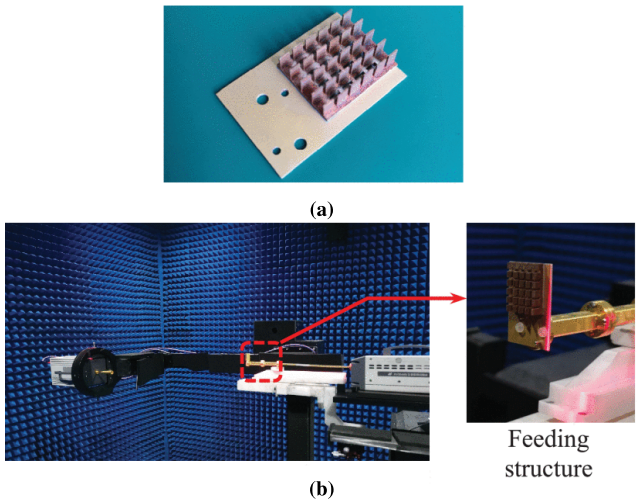

FIGURE 27. (a) Fabricated heatsink antenna and, (b) measurement setup in mm-wave anechoic chamber (images extracted from [35]).

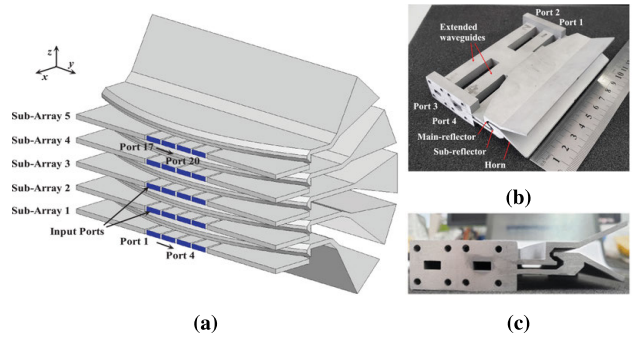

FIGURE 28. Multibeam Cassegrain antenna: (a) Perspective view of the model of the 2D array, (b) perspective view of the printed 1D subarray and, (c) side view of the 3D printed 1D subarray (images extracted from [36]).

common steps, namely selection, crossover, and mutation, were applied. Selection involved identifying individuals for reproduction, represented by 50 randomly generated boolean strings. These individuals, acting as parents, transmitted their genetic information to the next generation. Following selection, a script converted these individuals into simulated antennas, extracting parameters such as gain and S_{11}. The outcomes were then utilized in calculating a fitness function, integrating crossover to generate offspring from the combination of two distinct parents, and mutation to

TABLE 2. Summary table of 3D printed antennas and techniques.

Ref.	3D printing process	Antenna type	Material(s)	3D printer	Freq. of operation [GHz]	Bandwidth [GHz]	Gain
[9]	FDM/FFF	Microstrip patch	PLA/ Electrifi	Modified Ocular 3D	2.5	n/a	3 dBi
[9]		Horn antenna	Electrifi	Modified Ocular 3D	5.8	n/a	14.3 dBi
[10]		Dielectric resonator antenna	n/a	n/a	6.15	4.3 – 8.0	0.65 – 2.45 dBi ◇
[11]		Gradient index lens	ABS/PREPERM TP20280	Makerbot 2X	26	12 – 40	15.1 – 23.6 dBi ◇
[12]		Compact parabolic reflector antenna	PLA/aluminum foil/Rogers RT5880	Creality Ender 3	24.125	23.5 – 25.5	18.3 dBi
[13]		Curved patch antenna	ABS/aluminum foil	n/a	2.16	1.99 – 2.29 †	6.7 dBi
[14]		Spiral dielectric leaky wave antenna	PREPERM ABS300/ABS1000	Creality CP-01	18	16 – 20	25 dBi
[15]		MIMO dielectric resonator antenna	n/a	n/a	10	8.88 – 11.04	4 – 5 dBic ◇
[16]		Dual-band rectenna system (low-band)	Conformal PLA	n/a	2.4	2.05 – 2.75	5.7 dBi
[16]		Dual-band rectenna system (high-band)	Conformal PLA	n/a	5.2	4.915 – 5.485	8.8 dBi
[17]		Offset elliptic reflector antenna	ABS/MG Chemicals silver-coated copper spray	Snapmaker 2.0 A350	223 GHz	n/a	38.7 dBi
[18]	SLA	Slotted waveguide array	Formlabs black resin/Silver coating	Formlabs Form 2	78.68	78.5 – 79 †	22.5 dBi
[19]		Fresnel zone plane antenna	High-temperature resin	Formlabs Form 2	300	265 – 320 †	27.4 dBic
[20]		Dielectric helical antenna	>95% zirconia ceramic	CERAMAKER printer	6	4.75 – 9.5	10 dBic
[21]		Archimedean spiral antenna	Zirconia ceramic	PCPrinter DLP96F	5.1	4.75 – 6.1	9 dBic
[22]		Circular ME-dipole	VeroPureWhite/F4B/Copper and chromium foils	n/a	3.4	3.2 – 5.4	6.0 dBic
[22]		Circular ME-dipole 2×2 array	VeroPureWhite/F4B/Copper and chromium foils	n/a	3.4	3.2 – 5.2	14.0 dBic
[23]		Multibeam lens	High Temp resin/RT5880/CuClad217/Chromium foils	n/a	39	38.3 – 40	14.5 – 15.8 dBi ⋆
[24]		Gradient index lens	HTL resin/Gold coating	SLA nanoArch S140 printer	355	330 – 380	17.3 dBi ⋆
[25]	AJ-P	Microwave nail antenna	ABS/Cabot CS-32 silver ink	Optomec printer	15	14.5 – 15.9	6.4 dBi
[25]		Milimeter wave nail antenna	ABS/Cabot CS-32 silver ink and copper	Optomec printer	28	26.9 – 29.8	7.4 dBi
[26]		Stacked patch array antenna	Ferro A6M-E	n/a	140	127.65 – 160.41 †	7.1 dBi
[27]	Polyjet	3D printed transmitarray	VeroWhitePlus/RT-Duroid 6006	Objet30	30	n/a	30.7 dBi
[28]		Luneburg lens	VeroClear	n/a	33	26 – 40	21.2±2.5 dBi ‡
[29]		Cavity-backed patch antenna	Acrylate and silver nanoparticle conductive inks	n/a	28 †	26.9 – 31.7	5 – 7.8 dBi ⋆
[30]	LPBF	Pyramidal fractal antenna	Hoegenaes Cu OFCH	Trumpf TruPrint 1000 Green Edition	5.569	n/a	n/a
[31]		Conformal slotted waveguide antenna array	AlSi10Mg	AddUp Formup350	14.5	13.75 – 15	14 dBi
[32]		Evolutionary optimized WiFi Antennas	SLM Solution's AlSi10Mg	Custom Aconity3D AconityMIDI	2.462	2.27 – 2.58 †	3.27 dBi
[33]	DMLS	Horn 8×8 array	AlSi10Mg	n/a	32	28.2 – 35.8	27.5 dBi
[33]		Horn 16×16 array	AlSi10Mg	n/a	32	28.2 – 35.8	33.8 dBi
[35]		Heat sink antenna	Copper	n/a	60	55.73 – 62.73	18.1 dBi
[36]		Cassegrain beamformer	AlSi10Mg	BLT-S310	33	26 – 40	23 dBi

† - obtained through graphical data;
◇ - gain variation over the bandwidth;
⋆ - depending on the selected feeding patch;
∗ - gain at boresight;
‡ - peak gain and in-band variation;
n/a - not available.

introduce random genetic alterations in the population. The genetic algorithm's objective function focused on the mean value across specific frequencies (2.4, 2.45 and 2.5 GHz), incorporating rank-based fitness scaling to favor the best-performing individuals for reproduction. This iterative process continued until the predefined target was achieved. Subsequently, a voxelization and region-growing algorithm were implemented, complemented by the addition of a differential feed positioned between the first and second layers of the antenna. The manufacturing phase involved the use of SLM Solution's AlSi10Mg powder (Fig. 25a) with particle sizes ranging from 20 to 63 μm. A customized AconityMIDI LPBF printer was utilized for the printing process. In the measurement phase, the resonance frequency of the antenna was determined to be 2.462 GHz, accompanied by a bandwidth of 308.8 MHz and a peak gain of 3.27 dBi.

F. DMLS

Remarkably in [33], the authors present a 8 × 8 and 16 × 16 horn antenna array (HAA) in DMLS technology. The HAA consists of a four layer arrangement, composed by a H-plane waveguide feed network constructed on the bottom layer, short vertical waveguides that are connected to the radiating horn elements on the forth layer by a sub-feeding network (2 × 2 subarrays) present in the third layer. The horn antenna element was oriented vertically to improve radiation and fed by a horizontally terminated waveguide, with an additional part near the waveguide for impedance adjustment, as depicted in Fig. 26a. The proposed structure was 3D printed by DMLS using an aluminum alloy powder (AlSi10Mg) and heat-treated to prevent deformation. The prototype is shown in Fig. 26b. Measurements conducted in an anechoic chamber show that both arrays presented relatively good radiation performance, with cross-polarization levels below −30 dB for the 8 × 8 array and −40 dB for the 16 × 16 array. The 8 × 8 and 16 × 16 HAA designs had a wide impedance bandwidth of 23.8% (ranging from 28.2 to 35.8 GHz), with corresponding gains of 27.5 dBi and 33.8 dBi, in relatively good agreement with the ones obtained in simulation. Small differences are likely attributed to surface roughness. The authors suggest that horn radiating elements with an aperture size less than one wavelength in free space can effectively expand the operating bandwidth of the array. Further studies on a similar antenna design were recently presented by the same research group in [34], where modifications were made to enhance the bandwidth of the antenna array. Both studies highlighted the potential of DMLS in constructing complex multilayer millimeter-wave (mm-wave) antenna arrays.

In [35], a heatsink antenna array is designed and fabricated by combining 3D printing of copper and LTCC technologies. The proposed antenna comprises a 4 × 4 horn apertures implemented directly in a 3D printed copper heatsink, and a feeding network implemented as substrate integrated waveguide in the LTCC substrate. Simulations of the antenna are conducted in HFSS, where a stepped transition

structure was designed to improve the coupling between the antenna elements and feeding network embedded in the LTCC substrate. COMSOL simulations are also presented to study the temperature distribution and heat dissipation. The prototype of the antenna is depicted in Fig. 27. Although the authors do not mention the 3D printing technique used in the heatsink fabrication, we assume either SLM or DMLS techniques was employed. According to experimental results obtained in the prototype, both antenna matching (S_{11}) and broadside gain are in relatively good agreement with the simulation ones. The antenna presents a measured broadside gain of 18.1 dBi at 60 GHz, with a −10 dB impedance bandwidth set from 55.73 to 62.73 GHz. The HPBW is of 15° and 16° for the E and H-planes, respectively.

The article referenced as [36] presents a wideband planar Cassegrain beamformer produced using DMLS technology. In this design, the sub-reflector was changed to a concave geometry to reduce the profile of the boresight direction. The antenna design consisted of an air-filled open-ended rectangular waveguide located in the bottom layer, which was connected to a dual-reflector comprising folded waveguides in a 180° configuration. The flare was then connected at the end of the dual-reflector to enable radiation. To achieve 1D multibeam radiation, it was required to offset the feeding waveguide from the main reflector, which also enhanced impedance matching and expanded the −10 dB impedance bandwidth to more than 40%. To accomplish 2D multibeam radiation, the 1D Cassegrain design was stacked five times, as illustrated in Fig. 28. A prototype of the antenna was produced in a BLT-S310 machine with a resolution varying between 20 to 100 μm with a tolerance of 0.1 μm, using AlSi10Mg powder as the material. Measurements carried out in the prototype of the antenna are in good agreement between simulation. A standard gain horn antenna was used to measure gain, which reached 23 dBi at its peak with less than a 3 dB variation across the operating band. To summarize, the adoption of a concave subreflector led to a 20% reduction in the reflector's boresight direction. Even though the complete 2D array was not printed, a single subarray exhibited a radiation efficiency of over 90%.

V. CONCLUSION

Advancements in 3D printing technology have opened up new possibilities for antenna design and fabrication. The studies presented in this collection demonstrate the potential of 3D printed antennas to achieve desired characteristics such as wide bandwidth, high gain, circular polarization, and beamforming capabilities. The choice of materials plays a crucial role in the performance of 3D printed antennas. Researchers have explored multiple materials with different dielectric properties, such as ceramics, polymers, and composites, to optimize antenna performance at specific frequencies. Material selection involves a trade-off between dielectric properties, ease of printing, and compatibility with the printing process. The design of 3D printed antennas requires careful consideration of factors such as unit-cell dimensions, feed structures, and geometries. Simulation tools like HFSS, CST MWS and others have been used to analyze and optimize antenna designs, taking into account parameters such as impedance bandwidth, radiation patterns, gain, and efficiency. Iterative design processes have led to improved antenna performance and enhanced the understanding of the complex interactions between design parameters. The process of fabrication for 3D printed antennas involves selecting appropriate printing techniques and optimizing printing parameters to achieve the desired antenna structure. FDM, SLA, and DMLS are among the most commonly used 3D printing methods for antenna fabrication. Measurement and validation of 3D printed antennas are crucial to assess their performance and compare results with simulation predictions. VNA measurements and far-field chamber tests have been conducted to evaluate parameters such as reflection coefficients, radiation patterns, gain, and efficiency. Discrepancies between simulation and measurement results can be attributed to limitations in printing resolution, material properties, and non-ideal measurement conditions. The studies also highlight the limitations and challenges associated with 3D printed antennas. These include the availability of materials with suitable dielectric properties for specific frequencies, the resolution limitations of 3D printers, and manufacturing constraints at high frequencies.

Future research should focus on developing new materials with improved dielectric properties, refining printing techniques to enhance resolution and accuracy, while exploring innovative designs to further advance the capabilities of 3D printed antennas. greenBased on the insights gathered from the literature, it is evident that the landscape of 3D printing offers a plethora of options in terms of materials and techniques, especially as single-material and single-format 3D printing. Numerous commercially available options cater to these applications. However, when delving into the amalgamation of different materials, the scenario shifts, often requiring the utilization of custom-fabricated machines. This is particularly noticeable when aiming to create sophisticated composite solutions, such as embedding fiber threads in polymeric filaments or incorporating metal powders into polymeric filaments or pellets. While custom machine fabrication offers a viable approach to crafting composites, it brings forth potential challenges. The construction process may be constrained by budget limitations, leading to compromises in selecting the most suitable materials and components for their creation. Consequently, this could introduce additional degrees of error. An emerging frontier in the domain of 3D printing, intersecting both materials and techniques, is the rapidly evolving field of four-dimensional (4D) printing. In 4D printing, smart materials are employed, introducing a fourth variable that allows these to programmatically alter their properties over time. This innovative approach holds promise for dynamic and adaptive structures. In the context of dielectric type antennas, existing limitations stem from their inherent volumetric structural anisotropy. This directly impacts the dielectric

properties of the material, influencing signal propagation in different axes. For metal type antennas, such as horns or reflectors, conductivity plays an important role as it ensures minimized surface resistance, reduces unintended scattering, and maximizes radiation, thereby enhancing efficiency. Considerations extend to surface roughness conforming to at least 1/8 of the smallest wavelength used in the antenna, following Rayleigh's principle. Depending on the antenna type, surface roughness may cause additional undesirable delays in dielectric materials and scattering on metal surfaces. The resolution and accuracy of the employed 3D printer plays a pivotal role in addressing and improving these aspects, gaining prominence particularly as applications operate at increasingly higher frequencies. Despite the challenges, the results presented in these studies demonstrate the potential of 3D printed antennas for a wide range of applications in wireless communication systems, terahertz frequencies, transmitarrays, multibeam systems, and more.

REFERENCES

[1] *Additive Manufacturing—General Principles—Fundamentals and Vocabulary*, Standard ISO/ASTM 52900, International Organization for Standardization, 2021.

[2] D. Bourell, J. Beaman, and T. Wohlers, "History of additive manufacturing," in *Additive Manufacturing Processes*. ASM International, Jun. 2020. [Online]. Available: https://dl.asminternational.org/book/chapter-pdf/511836/a0006548.pdf and https://doi.org/10.31399/asm.hb.v24.a0006548

[3] J. Izdebska-Podsiadly, C. Pal, A. Krishnamoorthy, B. Banjanin, G. Vladic, S. Adamovic, and G. Bosnjakovic, *Polymers for 3D Printing: Methods, Properties, and Characteristics* (Plastics Design Library), J. Izdebska-Podsiadly, Ed. OH, USA: ASM International, 2022, ch. 1–3. [Online]. Available: https://www.asminternational.org/about-asm/contact/publish/

[4] J. K. Fink, *3D Industrial Printing With Polymers*. Hoboken, NJ, USA: Wiley, 2019.

[5] S. L. Marasso and M. Cocuzza, *High Resolution Manufacturing From 2D to 3D/4D Printing: Applications in Engineering and Medicine*. Berlin, Germany: Springer, 2022.

[6] R. Singh, B. S. Dhaliwal, and S. S. Pattnaik, *3D Printing of Sensors, Actuators, and Antennas for Low-Cost Product Manufacturing* (Sustainable Manufacturing Technologies: Additive, Subtractive, and Hybrid). Boca Raton, FL, USA: CRC Press, 2022.

[7] T. Kerr, "3D printing," in *Synthesis Lectures on Digital Circuits & Systems*. Cham, Switzerland: Springer, 2022. [Online]. Available: https://link.springer.com/book/10.1007/978-3-031-19350-7 and https://www.local.ch/en/d/cham/6330/springer-international-publishing-ag-1fEftmL9uw9VwKyeQarEsg

[8] M. Anand and A. K. Das, "Issues in fabrication of 3D components through DMLS technique: A review," *Opt. Laser Technol.*, vol. 139, Jul. 2021, Art. no. 106914. [Online]. Available: https://www.sciencedirect.com/science/article/pii/S0030399221000025

[9] F. Pizarro, R. Salazar, E. Rajo-Iglesias, M. Rodríguez, S. Fingerhuth, and G. Hermosilla, "Parametric study of 3D additive printing parameters using conductive filaments on microwave topologies," *IEEE Access*, vol. 7, pp. 106814–106823, 2019.

[10] Z.-X. Xia, K. W. Leung, and K. Lu, "3-D-printed wideband multi-ring dielectric resonator antenna," *IEEE Antennas Wireless Propag. Lett.*, vol. 18, no. 10, pp. 2110–2114, Oct. 2019.

[11] S. Zhang, R. K. Arya, W. G. Whittow, D. Cadman, R. Mittra, and J. C. Vardaxoglou, "Ultra-wideband flat metamaterial GRIN lenses assisted with additive manufacturing technique," *IEEE Trans. Antennas Propag.*, vol. 69, no. 7, pp. 3788–3799, Jul. 2021.

[12] J. R. Reis, C. Ribeiro, and R. F. S. Caldeirinha, "Compact 3D-printed reflector antenna for radar applications at K-band," *IET Microw., Antennas Propag.*, vol. 15, no. 8, pp. 843–854, Jul. 2021. [Online]. Available: https://ietresearch.onlinelibrary.wiley.com/doi/abs/10.1049/mia2.12095

[13] G. Muntoni, G. Montisci, A. Melis, M. B. Lodi, N. Curreli, M. Simone, G. Tedeschi, A. Fanti, T. Pisanu, I. Kriegel, A. Athanassiou, and G. Mazzarella, "A curved 3D-printed S-band patch antenna for plastic CubeSat," *IEEE Open J. Antennas Propag.*, vol. 3, pp. 1351–1363, 2022.

[14] T. Lira-Valdés, E. Rajo-Iglesias, and F. Pizarro, "3-D-printed spiral leaky wave antenna with circular polarization," *IEEE Open J. Antennas Propag.*, vol. 4, pp. 427–433, 2023.

[15] C. Yang and K. W. Leung, "3-D-Printed wideband circularly polarized MIMO dielectric resonator antenna," *IEEE Trans. Antennas Propag.*, vol. 71, no. 7, pp. 5675–5683, Jul. 2023.

[16] D. D. Patil, K. S. Subramanian, and N. C. Pradhan, "3-D-printed dual-band rectenna system for green IoT application," *IEEE Trans. Circuits Syst. II, Exp. Briefs*, vol. 70, no. 8, pp. 2864–2868, 2023.

[17] A. V. Muppala, A. Alburadi, A. Y. Nashashibi, H. N. Shaman, and K. Sarabandi, "A 223-GHz FMCW imaging radar with 360° FoV and 0.3° azimuthal resolution enabled by a rotationally stable fan-beam reflector," *IEEE Trans. Geosci. Remote Sens.*, vol. 61, pp. 1–9, 2023.

[18] J. Tak, A. Kantemur, Y. Sharma, and H. Xin, "A 3-D-printed W-band slotted waveguide array antenna optimized using machine learning," *IEEE Antennas Wireless Propag. Lett.*, vol. 17, no. 11, pp. 2008–2012, Nov. 2018.

[19] G.-B. Wu, Y.-S. Zeng, K. F. Chan, S.-W. Qu, and C. H. Chan, "3-D printed circularly polarized modified Fresnel lens operating at terahertz frequencies," *IEEE Trans. Antennas Propag.*, vol. 67, no. 7, pp. 4429–4437, Jul. 2019.

[20] S. Wang, L. Zhu, Y. Li, G. Zhang, J. Yang, J. Wang, and W. Wu, "Radar cross-section reduction of helical antenna by replacing metal with 3-D printed zirconia ceramic," *IEEE Antennas Wireless Propag. Lett.*, vol. 19, no. 2, pp. 350–354, Feb. 2020.

[21] S. Wang, F. Fan, Y. Xu, Z.-C. Guo, W. Zheng, Y.-T. Liu, and Y. Li, "3-D printed zirconia ceramic Archimedean spiral antenna: Theory and performance in comparison with its metal counterpart," *IEEE Antennas Wireless Propag. Lett.*, vol. 21, no. 6, pp. 1173–1177, Jun. 2022.

[22] B. Feng, L. Li, K. L. Chung, and Y. Li, "Wideband widebeam dual circularly polarized magnetoelectric dipole antenna/array with meta-columns loading for 5G and beyond," *IEEE Trans. Antennas Propag.*, vol. 69, no. 1, pp. 219–228, Jan. 2021.

[23] K. Trzebiatowski, W. Kalista, M. Rzymowski, L. Kulas, and K. Nyka, "Multibeam antenna for Ka-band CubeSat connectivity using 3-D printed lens and antenna array," *IEEE Antennas Wireless Propag. Lett.*, vol. 21, no. 11, pp. 2244–2248, Nov. 2022.

[24] B. Nie, H. Lu, T. Skaik, Y. Liu, and Y. Wang, "A 3D-printed subterahertz metallic surface-wave Luneburg lens multibeam antenna," *IEEE Trans. Terahertz Sci. Technol.*, vol. 13, no. 3, pp. 297–301, May 2023.

[25] P. Njogu, B. Sanz-Izquierdo, A. Elibiary, S. Y. Jun, Z. Chen, and D. Bird, "3D printed fingernail antennas for 5G applications," *IEEE Access*, vol. 8, pp. 228711–228719, 2020.

[26] M. Ihle, S. Ziesche, C. Zech, and B. Baumann, "A broadband 140 GHz aperture-coupled SPA antenna in LTCC-technology," in *Proc. 53rd Eur. Microw. Conf. (EuMC)*, Sep. 2023, pp. 327–330.

[27] A. Massaccesi, P. Pirinoli, V. Bertana, G. Scordo, S. L. Marasso, M. Cocuzza, and G. Dassano, "3D-printable dielectric transmitarray with enhanced bandwidth at millimeter-waves," *IEEE Access*, vol. 6, pp. 46407–46418, 2018.

[28] Y. Li, L. Ge, M. Chen, Z. Zhang, Z. Li, and J. Wang, "Multibeam 3-D-printed Luneburg lens fed by magnetoelectric dipole antennas for millimeter-wave MIMO applications," *IEEE Trans. Antennas Propag.*, vol. 67, no. 5, pp. 2923–2933, May 2019.

[29] J. Qin, J. Li, Y. Lu, S. Chen, K.-D. Hong, and T. Yuan, "A monolithically polyjet 3-D printed millimeter-wave quasi-planar air-filled cavity-backed patch antenna with enhanced gain," in *Proc. 53rd Eur. Microw. Conf. (EuMC)*, 2023, pp. 690–693.

[30] K. Johnson, E. Burden, M. Shaffer, T. Noack, M. Mueller, J. Walker, E. MacDonald, P. Cortes, and J. Quintana, "A copper pyramidal fractal antenna fabricated with green-laser powder bed fusion," *Prog. Additive Manuf.*, vol. 7, no. 5, pp. 931–942, Oct. 2022, doi: 10.1007/s40964-022-00268-9.

[31] C. Stoumpos, T. L. Gouguec, R. Allanic, M. García-Vigueras, and A.-C. Amiaud, "Compact additively manufactured conformal slotted waveguide antenna array," *IEEE Antennas Wireless Propag. Lett.*, vol. 22, no. 8, pp. 1843–1847, 2023.

[32] D. Mair, M. Renzler, S. Kovar, T. Martinek, T. Kadavy, S. Bergmueller, A. Horn, J. Braun, and L. Kaserer, "Evolutionary optimized 3D WiFi antennas manufactured via laser powder bed fusion," *IEEE Access*, vol. 11, pp. 121914–121923, 2023.

[33] Y. Li, L. Ge, J. Wang, S. Da, D. Cao, J. Wang, and Y. Liu, "3-D printed high-gain wideband waveguide fed horn antenna arrays for millimeter-wave applications," *IEEE Trans. Antennas Propag.*, vol. 67, no. 5, pp. 2868–2877, May 2019.
[34] F. Sun, Y. Li, J. Wang, L. Ge, J. Chen, and W. Qin, "Bandwidth enhancement of millimeter-wave large-scale antenna arrays using X-type full-corporate waveguide feed networks," *IEEE Open J. Antennas Propag.*, vol. 3, pp. 1044–1056, 2022.
[35] J. Qian, M. Tang, Y.-P. Zhang, and J. Mao, "Heatsink antenna array for millimeter-wave applications," *IEEE Trans. Antennas Propag.*, vol. 68, no. 11, pp. 7664–7669, Nov. 2020.
[36] Y. Bi, Y. Li, and J. Wang, "3-D printed wideband Cassegrain antenna with a concave subreflector for 5G millimeter-wave 2-D multibeam applications," *IEEE Trans. Antennas Propag.*, vol. 68, no. 6, pp. 4362–4371, Jun. 2020.

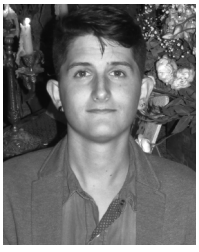

SAÚL S. CARVALHO received the bachelor's degree in electrical engineering, specializing in electronics and telecommunications, from the School of Technology and Management (ESTG), Polytechnic Institute of Leiria (IPL), Portugal, in 2022, where he is currently pursuing the Ph.D. degree in electrical engineering. In 2022, he also had the honor of being invited to lecture at ESTG, IPL, while pursuing the master's degree. Since then, he has been a Researcher with the Instituto de Telecomunicações, Portugal, specifically within the Group of Antennas and Propagation Leiria (A&P-Lr). His research interests include antennas and radio wave propagation, with a specific emphasis on the development of antennas using 3D printing technologies.

JOÃO R. V. REIS was born in Lisbon, Portugal, in 1987. He received the bachelor's and master's degrees in electrical engineering, electronics and telecommunications from the School of Technology and Management (ESTG), Polytechnic Institute of Leiria (IPL), Portugal, in 2010 and 2013, respectively, and the Ph.D. degree in electrical engineering (antennas and propagation) from the University of South Wales, Treforest, U.K., with a focus on "Novel Antenna Beamsteering for Wireless Applications." He is currently a Contract Researcher with ESTG, IPL working on the project INOV.AM, and a Researcher with the Group of Antennas and Propagation Leiria (A&P-Lr), Instituto de Telecomunicações, Portugal, participating in several international projects. He is also an Invited Lecturer with ESTG, IPL, lecturing and (co-) supervising several bachelor's final year projects and master's dissertations. He has contributed to the literature with two granted patents, ten articles publications in highly reputed international journals, a contribution to one book chapter, and several international peer-reviewed conference publications. His current research interests include antennas (smart antennas, 3D and 4D printed antennas), radio wave propagation, beam steering systems, frequency selective surfaces (FSS), metamaterials, transmit- and receive-reconfigurable intelligent surfaces (T-RIS, R-RIS), and smart radio environments. He is a Reviewer for several top international journals in the field of antennas and propagation, such as IEEE Transactions on Antennas and Propagation, *IET Microwaves, Antennas and Propagation*, and *International Journal of Communication Systems* (Wiley).

ARTUR MATEUS received the degree in mechanical engineering from the Faculty of Sciences and Technology, University of Coimbra, the master's degree in mechanical engineering from Instituto Superior Técnico, University of Lisbon (IST-UL), and the Ph.D. degree from the Department of Physics, University of Reading, U.K. He is currently an Adjunct Professor with the Department of Mechanical Engineering, School of Technology and Management (ESTG), Polytechnic of Leiria (IPL), carrying out research and teaching in the areas of advanced production technologies, additive manufacturing, computer-aided engineering, virtual prototyping, computational modeling and simulation, augmented reality, rapid tool manufacturing, and product design and development. He is also the Director of the Centre for Rapid and Sustainable Product Development (CDRSP), IPL. He is the co-editor of 11 books, the author, or the coauthor of more than 100 articles in international magazines, national magazines, book chapters, book articles, and conference proceedings, and the coauthor of 17 patents and two industrial models. Over the last 14 years, he has collaborated in the implementation of around 230 national and international research projects mainly in the direct digital manufacturing area. Since September 2016, he has been a member of the Technological and Advisory Board of the Business Incubator-Association for Specific Business Opportunities (OPEN).

RAFAEL F. S. CALDEIRINHA (Senior Member, IEEE) was born in Leiria, Portugal, in 1974. He received the B.Eng. degree (Hons.) in electronic and communication engineering and the Ph.D. degree from the University of Glamorgan, U.K., in 1997 and 2001, respectively, and the Habilitation (Agregação) degree from the University of Aveiro, Portugal, in 2020. He has been a Senior Researcher and the Head of the Antennas and Propagation (A&P-Lr) Research Group, Instituto de Telecomunicações, Leiria, since 2010, and a Coordinator Professor in mobile communications with the Polytechnic of Leiria, since 2001. He has authored or coauthored more than 200 papers in conferences and international journals, two national patents, and four contributions to the ITU-R Study Group, which formed the basis of the ITU-R P.833-5 (2005) recommendation. His research interests include studies of radio wave propagation through vegetation media, including wildfires, radio channel sounding and modeling, and frequency-selective surfaces, for applications at micro- and millimeter-wave frequencies. He is a Senior Member of URSI and a fellow of IET. He was an Associate Editor of IEEE TRANSACTIONS ON ANTENNAS AND PROPAGATION journal, from 2016 to 2022; an Associate Editor of the *IET on Microwaves, Antennas and Propagation* journal; a member of the editorial board of the *International Journal of Communication Systems*, (New York, Wiley); the Program Chair of the WINSYS International Conference, from 2006 to 2012; an Appointed Officer of Awards and Recognitions of the IEEE Portugal Section, in 2014; the Chair of the IEEE Portugal Joint Chapter on Antennas and Propagation-Electron Devices-Microwave Theory and Techniques, from 2016 to 2021; a Regional Delegate of the European Association for Antennas and Propagation (EurAAP) for Andorra, Portugal, and Spain, from 2017 to 2023; and a Member of Board of Directors, since 2023.